

Perforated Mach-Zehnder Interferometer Evanescent Field Sensor in Silicon-on-Insulator

by

KSENIA YADAV

B. A. Sc. (Waterloo) 2004

A Thesis

Submitted to the Faculty of Graduate Studies and Research
in Partial Fulfillment of the Requirements
for the Degree of
Master of Applied Science

Ottawa-Carleton Institute for Electrical and Computer Engineering
Department of Electronics
Carleton University
Ottawa, Ontario, Canada

September 2006

©Copyright by Ksenia Yadav, 2006.



Library and
Archives Canada

Bibliothèque et
Archives Canada

Published Heritage
Branch

Direction du
Patrimoine de l'édition

395 Wellington Street
Ottawa ON K1A 0N4
Canada

395, rue Wellington
Ottawa ON K1A 0N4
Canada

Your file *Votre référence*
ISBN: 978-0-494-18335-9
Our file *Notre référence*
ISBN: 978-0-494-18335-9

NOTICE:

The author has granted a non-exclusive license allowing Library and Archives Canada to reproduce, publish, archive, preserve, conserve, communicate to the public by telecommunication or on the Internet, loan, distribute and sell theses worldwide, for commercial or non-commercial purposes, in microform, paper, electronic and/or any other formats.

The author retains copyright ownership and moral rights in this thesis. Neither the thesis nor substantial extracts from it may be printed or otherwise reproduced without the author's permission.

AVIS:

L'auteur a accordé une licence non exclusive permettant à la Bibliothèque et Archives Canada de reproduire, publier, archiver, sauvegarder, conserver, transmettre au public par télécommunication ou par l'Internet, prêter, distribuer et vendre des thèses partout dans le monde, à des fins commerciales ou autres, sur support microforme, papier, électronique et/ou autres formats.

L'auteur conserve la propriété du droit d'auteur et des droits moraux qui protègent cette thèse. Ni la thèse ni des extraits substantiels de celle-ci ne doivent être imprimés ou autrement reproduits sans son autorisation.

In compliance with the Canadian Privacy Act some supporting forms may have been removed from this thesis.

Conformément à la loi canadienne sur la protection de la vie privée, quelques formulaires secondaires ont été enlevés de cette thèse.

While these forms may be included in the document page count, their removal does not represent any loss of content from the thesis.

Bien que ces formulaires aient inclus dans la pagination, il n'y aura aucun contenu manquant.


Canada

Abstract

This thesis investigates an evanescent field refractive index sensor based on a planar waveguide silicon-on-insulator (SOI) unbalanced Mach-Zehnder interferometer structure. The key element used for enhancing the sensitivity of the device is a waveguide structure that contains perforations through its core guiding layer.

Three-dimensional numerical solution of the wave equation was used to determine optimal device dimensions and model device behavior. Devices were then fabricated in 3.4 μm thick SOI material and optically characterized. It was found that the perforations in the waveguide increased its sensitivity to refractive index changes in the cladding by a factor of two. The sensitivity was calculated to be 2.2 nm shift in the interferometer output spectrum per unit refractive index change of the cladding. It is expected that further optimization of the perforated waveguide structure will result in a significant increase in sensitivity.

Acknowledgements

I would like to thank my supervisor, Professor Garry Tarr, for his guidance and support during my graduate studies. I also want to express my gratitude to Phil Waldron, who provided invaluable advice and knowledge on many occasions throughout this project.

I received a lot of help with the fabrication of my devices. Sincere thanks to Rob Vandusen for his enthusiastic response to my endless requests to set up one thing or the other, to Carol Adams for her positive attitude and frequent help in the lab, to Khaled Mnaymneh for his invaluable help during my first few weeks in the lab, to Chris Raum for sharing his legendary cleaving skills, and to Andrew McCarthy for help with fabricating the sensing-windows mask.

The simulation work that was done in this project seemed to require insatiable resources. Many thanks to Nagui Mikhail, who did everything in his effort and beyond to find computer stations that were capable of running my simulations. I also want to thank Scott Bruce, who was very patient with my unending requests for software installations and license keys.

I would like to thank the National Research Council Institute for Microstructural Sciences for allowing me to do the optical characterization of my devices in their lab. A special thank you goes to Edith Post for great help with the optical measurements. During the measurement phase of my project, I also received extremely invaluable and timely advice from Professor John Gaydos.

I want to thank Winnie Ye for her advice on many occasions and more importantly for her friendship, and to Yanina Shevchenko for her enthusiasm, encouragement and the blissful breaks we took together during the past year. A special thank you to my parents for their guidance and encouragement. Finally and most of all, I want to thank my husband, Bhupendra, for being an unwavering source of support and energy in my life.

Contents

List of Figures	vi
List of Tables	viii
1 Introduction	1
1.1 Optical Sensor Technology	2
1.2 Thesis Contribution	7
1.3 Thesis Organization	7
2 Theoretical Background	9
2.1 Optical Waveguide Theory	9
2.1.1 Electromagnetic Propagation	9
2.1.2 One-Dimensional Confinement	11
2.1.3 Two-Dimensional Confinement	14
2.2 Mach-Zehnder Interferometer	16
2.3 Liquid Dynamics	22
3 Design and Simulation	25
3.1 Waveguide Structure	25
3.2 Waveguide Perforations	27
3.2.1 Dimensions of the Perforations	30
3.2.2 Average Propagation Constant	32
3.2.3 Optical Loss	40
3.3 Mach-Zehnder Interferometer	40
3.4 Summary of Simulation Results	45
4 Fabrication	47
4.1 Materials	47
4.2 Fabrication Process	48

5	Experimental Results	62
5.1	Measurement Setup	62
5.2	Waveguide Measurements	63
5.3	Unbalanced Mach-Zehnder Interferometer Measurements	65
5.4	Discussion of Results	72
6	Conclusions and Recommendations	78
A	List of Acronyms	81
B	Device Process Flow	83
	Bibliography	85

List of Figures

1.1	Silicon-on-insulator material for optical waveguides.	4
2.1	Slab waveguide structure.	11
2.2	Normalized b - V diagram for the first three TE slab waveguide modes for several values of the asymmetry parameter.	14
2.3	Silicon-on-insulator slab waveguide.	15
2.4	Rib waveguide analysis.	16
2.5	Buried oxide layer thickness versus silicon-on-insulator waveguide thickness for achieving leakage losses below 0.001 dB/cm for the fundamental TE and TM modes.	17
2.6	Balanced Mach-Zehnder interferometer structure.	18
2.7	Unbalanced Mach-Zehnder interferometer structure.	20
2.8	Examples of pore structures.	23
2.9	Example of the two-stage pore filling process.	24
3.1	FIMMWAVE two-dimensional mode solver simulation results, showing the intensity distribution of the supported modes of the waveguide structure.	27
3.2	Simulation setup of the perforated waveguide.	28
3.3	The effect of perforation depth on the average effective index of the fundamental TM mode and the optical power remaining at the end of a 9 μm long perforated waveguide.	33
3.4	FIMMWAVE two-dimensional mode solver simulation results, showing the intensity distribution of the fundamental TM mode in selected waveguide cross-sections for air and water upper cladding.	34
3.5	OptiFDTD three-dimensional simulation results for 9 μm long waveguide structures.	37
3.6	FIMMPROP three-dimensional simulation results for 9 μm long waveguide structures.	38
3.7	The unbalanced Mach-Zehnder interferometer structure used in this project.	41

3.8	OptiBPM simulation of field propagation in the unbalanced Mach-Zehnder interferometer.	42
3.9	APSS simulation of output intensity as a function of input wavelength in the unbalanced Mach-Zehnder interferometer.	43
3.10	MATLAB simulation of the unbalanced Mach-Zehnder interferometer spectrum shift when measurand is changed from air to water.	44
3.11	Summary of device dimensions.	45
3.12	Summary of OptiFDTD and FIMMPROP average effective index simulation results.	46
4.1	Perforations pattern designed for the SEM control software.	49
4.2	SEM pictures of etched perforation test structures.	52
4.3	Layout of the waveguide-structures mask.	53
4.4	SEM pictures of a fabricated rib waveguide.	55
4.5	SEM picture of a fabricated perforated rib waveguide.	56
4.6	Layout of the sensing-windows mask.	60
5.1	National Research Council optical measurement setup.	63
5.2	Measured power spectra of a standard waveguide and a perforated waveguide.	65
5.3	Measured power spectrum of the perforated Mach-Zehnder interferometer with air as upper cladding.	69
5.4	Measured power spectra of the perforated Mach-Zehnder interferometer with air and water as upper cladding.	70
5.5	Simulated sensor device behavior for measurands with different refractive indices.	74

List of Tables

3.1	Refractive index values used in simulations.	26
3.2	Expected relationships between the average effective indices for the four simulated waveguide structures.	35
3.3	Average effective index results based on OptiFDTD simulations.	36
3.4	Average effective index results based on FIMMPROP simulations.	40
3.5	Geometrical parameters of the unbalanced Mach-Zehnder interferometer.	41
4.1	Nominal specifications of the SOI SmartCut wafers used in device fabrication.	48
4.2	Electron-beam lithography SEM settings.	50
4.3	Descum oxygen plasma process settings.	50
4.4	ECR etcher settings.	51
4.5	Dimensions of the devices on the waveguide-structures mask.	53
4.6	Mask aligner settings.	54
4.7	Grinding wheel settings.	58

Chapter 1

Introduction

The importance of sensor technology stems from the many applications of sensing in environmental, medical, agricultural, military and other industries. Sensors translate quantities to be measured into signals that can be readily transmitted and processed to provide information needed to support a diversity of systems. The requirements for a specific sensor vary largely depending on its application, however, some common desired properties include high sensitivity in the required range of operation, geometric versatility, immunity to environmental noise, small size and low cost.

This chapter begins by introducing optical sensors and outlining their advantages compared to other, more-established sensor technologies. The operation of planar waveguide-based evanescent field sensors is explained, with special emphasis on sensors implemented on a silicon-on-insulator (SOI) platform. The different approaches to measuring the changes detected by the sensor are briefly introduced, and latest developments in SOI evanescent field sensors are presented. Section 1.2 ties the current project into the recent work on planar waveguide-based evanescent field sensors, and outlines the goals of this project. Lastly, Section 1.3 describes the organization of this thesis and the material presented in the following chapters.

1.1 Optical Sensor Technology

Research and development in the optical sensor field is motivated by the following significant advantages of optical sensors compared to conventional sensors [1]:

- immunity to electromagnetic interference means that heavy shielding, which is often used for conventional electrical sensors, is not required;
- all-passive dielectric structure allows for elimination of conductive paths in high-voltage environments and electrical isolation of the measured system;
- environmental ruggedness allows for usage in high voltage, electrically noisy, high temperature, corrosive and other stressing environments;
- geometric versatility allows for all-solid configuration capable of withstanding extreme vibration and shock levels;
- small geometry and light weight of the sensing element allow for minimal footprint;
- inherent compatibility with standard optical fiber telecommunication technology allows for efficient transport of the optical signals;
- compatibility with large commercial telecommunication and optoelectronics markets allows for a substantial reduction in cost.

Modern optical sensors typically rely on fiber optics or planar waveguide optics. Fiber optic sensors allow the physical parameter to be measured, known as the measurand, to interact with the fiber or some device attached to the fiber to modulate the optical characteristics of a transmitted signal. One of the major advantages of fiber optic sensors is that they are inherently compatible with the optical fibers that are used for telecommunication, thus avoiding the need to develop advanced structures for efficient light coupling into and out of the sensor devices.

Planar waveguide-based optical sensors refer to structures in which the measurand interacts with light that is guided in a thin film optical waveguide. The great promise

of integrated optics is the ability to combine various optical components such as light sources, detectors, modulators, switches, optical sensors, etc. on a common substrate, and to link all the components by optical waveguides. In contrast to fiber optics, planar waveguide-based optics has greater flexibility in choosing the materials and structures of the optical system, thus giving additional freedom in the design process. Moreover, high-density integration of multiple components allows one to build sensor arrays on a single optical chip, creating a multi-purpose sensing system. However, efficient light coupling between a typical waveguide and a standard optical fiber, which is used to transmit the optical signal in and out of the waveguide-based device, has proven to be a major practical challenge.

In planar waveguide implementations of optical sensors, silicon technology has been of special interest for three main reasons. First, silicon processing techniques are mature and well-characterized thanks to the decades of research, development and manufacturing in the microelectronics industry. Second, the silicon platform has the potential for monolithic integration of optical and electrical components on the same substrate. Third, the high index contrast in silicon systems allows for compactness and high functional density, an important aspect for sensor array applications.

The majority of silicon photonic devices have been fabricated using the SOI platform. SOI is a generic term used to describe structures which consist of a thin layer of crystalline silicon on top of an insulating layer. The most common SOI structure is silicon-on-silica, in which a uniform layer of SiO_2 is sandwiched between a thick silicon substrate and a thin surface layer of crystalline silicon [2], as shown in Figure 1.1(a). SOI material was originally developed to improve the performance of electronics, where the buried oxide layer reduces junction capacitance to the silicon substrate, enabling operation at higher speeds with reduced power consumption [3]. For optics, the high index contrast of SOI allows for very small devices compared to other material systems, such as silica-on-silicon or III-V semiconductors. Optical waveguides in SOI allow propagation of light with photon energy below the bandgap of silicon (~ 1.12 eV [4], thus silicon is transparent for wavelengths greater than ~ 1.1 μm – the infra-red range and beyond), and the buried oxide layer provides optical confinement of the light in the thin high-index silicon film.

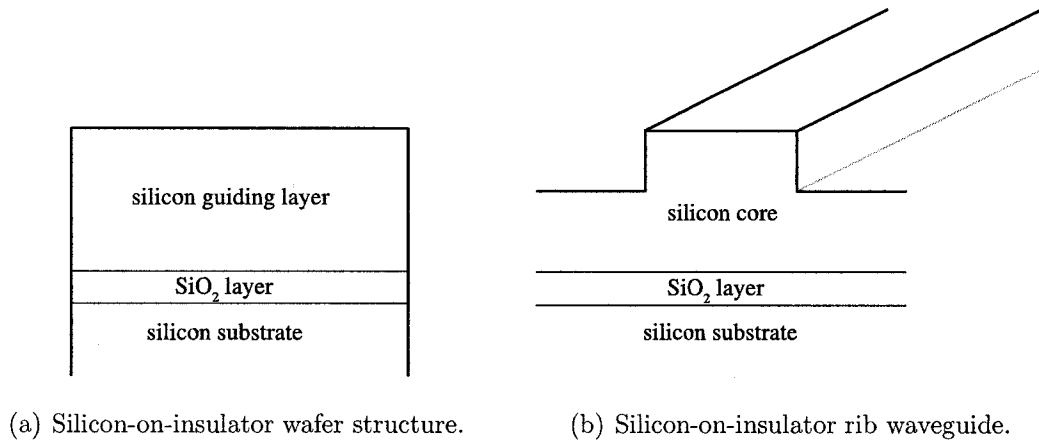


Figure 1.1: Silicon-on-insulator material for optical waveguides.

In order to realize an SOI waveguide that can guide an optical signal along a specified path, a three-dimensional rib waveguide structure, shown in Figure 1.1(b), is commonly used. In a rib waveguide, vertical confinement of the light signal is achieved by the higher refractive index of the core silicon layer compared to the indices of the SiO₂ and the upper cladding layers, and horizontal confinement is achieved by patterning a thicker rib region, as illustrated in Figure 1.1(b). This confinement in both vertical and horizontal directions keeps the optical signal within the silicon rib region as it propagates along the waveguide. In general, the waveguide geometry and the appropriate boundary conditions allow only a certain number of specific solutions to the wave equation that governs the propagation of light in the waveguide structure. These solutions are referred to as the *modes* of the structure. Each mode is characterized by its *effective index*, a parameter that can be thought of as the index of refraction that governs the electromagnetic wave as it propagates along the waveguide. It can be shown that the profiles of the mode fields must oscillate in the core guiding region and decay in an exponential fashion in the cladding regions. The portion of the mode that decays exponentially in the cladding of the waveguide structure is called the *evanescent field* of the mode.

Evanescent field sensing has been one of the most widely used methods for sensing in both fiber and planar waveguide-based optical sensor implementations. Because the

evanescent field travels outside the waveguide core, it can interact with the surrounding environment. When the cladding material undergoes a change in its refractive index, the evanescent field 'detects' this change, inducing a variation in the optical properties of the guided mode. Although only a fraction of the modal power actually experiences the change of the optical properties of the cladding, long interaction lengths allow for a significant cumulative effect. The effect of the measurand on the properties of the optical system is proportional to the fraction of the modal power which propagates through it. It is therefore desirable to increase the evanescent field in order to achieve greater sensor sensitivity.

Evanescent field sensing may rely on a change in one of three optical properties: the refractive index, the absorption coefficient or the emission properties of the measurand [5]. A change in the refractive index is expressed as a change in two parameters – the real part of the effective index and the mode field profile. A change of an absorption coefficient is expressed in the imaginary part of the effective index and thus in optical attenuation. The measurand material may also show luminescent properties, where part of the absorbed power is emitted as photons of another wavelength, generating a new mode.

The great majority of evanescent field sensors detect the change in the real part of the effective index of the propagating mode due to the introduction of the measurand into the optical system. The measurand can take different forms, from aqueous solutions of uniform refractive index to a thin layer of biological material on the waveguide surface. In order to measure the changes induced by the measurand, a number of structures can be exploited. One approach is to place the evanescent field sensor in an interferometer-based configuration, which relies on the interference between two signals, of which one is exposed to a variation in the optical properties of the cladding material, while the other is kept in a constant reference state. The interferometer-based structure that is most often used for evanescent field sensing is the Mach-Zehnder interferometer [6] [7] [8] [9], while other examples utilize the Young [10], Michelson [11] or difference [12] interferometer structures. Another approach that can be used to measure the change in the effective index induced by the measurand is to use a resonator-based system, where the optical signal passes

the sensing region multiple times, thus typically leading to larger effects than in interferometer-based structures. Examples of resonator-based evanescent field sensors include Fabry-Perot [13], ring [14] and disk [15] resonator implementations. Changes in the modal effective index can also be measured by observing the coupling between different modes, an approach used in grating assisted sensors [16] and sensors based on the surface plasmon resonance method [17].

At the time of writing, a number of research groups are working on SOI-based evanescent field sensors, however full description of the implementations has not yet been published. Although SOI-based sensor structures provide a number of advantages as outlined above, they also have the disadvantage that due to the high index contrast of the structure, the optical mode is tightly confined to the silicon guiding layer, and the fraction of the mode that is evanescent is very small. The general tendency in the current work on SOI evanescent field sensors has been to try and find a way to increase the interaction between the evanescent field and the measurand.

In [18] a sensor based on an SOI optical micro-ring resonator was presented. The resonator design allows the optical signal to pass the sensing region multiple times, thus resulting in greater interaction between the signal and the measurand. It is reported that the fabricated sensor is capable of detecting bulk refractive index changes of 7×10^{-3} .

In [19] high evanescent field was achieved by significantly reducing the size of the waveguide structure, at which point the guided mode becomes less confined within the waveguide core. Mach-Zehnder interferometer structures have been fabricated, achieving 411 nm per refractive index unit (RIU) wavelength shift in the transmission peak of the MZI for an interaction length of 1.5 mm, with $\sim 10^{-6}$ minimum detectable refractive index change. Note however that because of the very small waveguide dimensions (0.45 μm width, 0.26 μm thickness) of the fabricated sensors, challenges related to efficient coupling of light into and out of the devices are expected.

1.2 Thesis Contribution

The goal of this thesis is to design, fabricate and characterize an evanescent field refractive index sensor on silicon-on-insulator platform. One of the key design decisions of the proposed sensor is to keep the waveguide dimensions relatively large to facilitate efficient light coupling into and out of the sensor device. Since the evanescent field of such a large waveguide is very small, the expected sensitivity to variations in the refractive index of the cladding is also low, thus some mechanism is required to increase the interaction between the optical signal and the measurand, which is introduced as the cladding material of the waveguide. For this purpose, a randomly perforated waveguide structure is proposed, where the perforations are designed such that a larger portion of the mode field travels through the cladding material as evanescent field compared to a standard waveguide of the same dimensions. An unbalanced Mach-Zehnder interferometer has been chosen as the sensor device due to its relatively simple implementation and the availability of an appropriate mask for its fabrication. The sensor was realized by perforating the two arms of the interferometer, exposing one of the arms to different measurands while keeping the second arm in a constant reference state, and observing the intensity of the output signal. The effects of the perforations on the sensitivity of the sensor and the optical characteristics of the device are investigated using three-dimensional optical simulations and experimental measurements.

1.3 Thesis Organization

This thesis is divided into six chapters. Chapter 2 provides the theoretical background required to understand the material presented in the thesis, including the propagation of electromagnetic waves, the principle of operation of the Mach-Zehnder interferometer, and the behavior of liquids in perforated structures. Chapter 3 describes the design process used to obtain the chosen device parameters, and the simulations used to model the device behavior. In Chapter 4 the process and the equipment used in the fabrication of the device are outlined. Chapter 5 presents

the experimental measurements of the sensor, compares the experimental evidence to simulation results, and suggests a number of improvements to the current design. Chapter 6 concludes this thesis by summarizing the main results and providing recommendations for future work.

Chapter 2

Theoretical Background

This chapter provides the theoretical background required to understand the design and the operation of a perforated Mach-Zehnder interferometer sensor. Section 2.1 presents the fundamentals of light propagation, and the structures that can be used for one and two dimensional confinement of electromagnetic waves. Section 2.2 outlines the principle of operation of a Mach-Zehnder interferometer, and explains how the basic device is utilized for sensing in this project. Finally, Section 2.3 describes a two-stage model that can be used to characterize liquid behavior as it pertains to the proposed sensor device.

2.1 Optical Waveguide Theory

2.1.1 Electromagnetic Propagation

Propagation of light in a non-conducting, non-magnetic, isotropic, linear, dielectric and homogeneous medium can be described by the simplified Maxwell's equations

given by [20]:

$$\nabla \times E = -\mu_0 \frac{\partial \mathbf{H}}{\partial t} \quad (2.1)$$

$$\nabla \times H = \epsilon_0 n^2 \frac{\partial \mathbf{E}}{\partial t} \quad (2.2)$$

$$\nabla \cdot \mathbf{E} = 0 \quad (2.3)$$

$$\nabla \cdot \mathbf{H} = 0 \quad (2.4)$$

where \mathbf{E} and \mathbf{H} are the time-dependent vectors of the electric and magnetic fields, respectively, t is the time, μ_0 is the magnetic permeability of free space, ϵ_0 is the dielectric permittivity of free space, n is the refractive index, and ∇ is the del operator, defined as:

$$\nabla = \left(\frac{\partial \hat{\mathbf{x}}}{\partial x}, \frac{\partial \hat{\mathbf{y}}}{\partial y}, \frac{\partial \hat{\mathbf{z}}}{\partial z} \right) \quad (2.5)$$

where $\hat{\mathbf{x}}$, $\hat{\mathbf{y}}$ and $\hat{\mathbf{z}}$ are the unit vectors in the x , y and z directions, respectively.

Equations (2.1) – (2.4) can be combined to obtain the following equations for the electric and magnetic fields:

$$\nabla^2 \mathbf{E} = \epsilon_0 n^2 \mu_0 \frac{\partial^2 \mathbf{E}}{\partial t^2} \quad (2.6)$$

$$\nabla^2 \mathbf{H} = \epsilon_0 n^2 \mu_0 \frac{\partial^2 \mathbf{H}}{\partial t^2} \quad (2.7)$$

where ∇^2 is the Laplacian operator, given by:

$$\nabla^2 = \left(\frac{\partial^2}{\partial x^2} + \frac{\partial^2}{\partial y^2} + \frac{\partial^2}{\partial z^2} \right) \quad (2.8)$$

Equations (2.6) and (2.7) describe the propagation of electromagnetic waves, and thus are known as the *wave equations*. The general solutions to the wave equations for a wave propagating in an arbitrary direction $\mathbf{r} = (\hat{\mathbf{x}}x + \hat{\mathbf{y}}y + \hat{\mathbf{z}}z)$ are given by [21]:

$$\mathbf{E}(\mathbf{r}, t) = \mathbf{E}_0 e^{j(\omega t - \mathbf{k} \cdot \mathbf{r})} \quad (2.9)$$

$$\mathbf{H}(\mathbf{r}, t) = \mathbf{H}_0 e^{j(\omega t - \mathbf{k} \cdot \mathbf{r})} \quad (2.10)$$

where $\mathbf{E}_0 = (E_x \hat{\mathbf{x}} + E_y \hat{\mathbf{y}} + E_z \hat{\mathbf{z}})$ is the electric field amplitude of the wave, $\mathbf{H}_0 = (H_x \hat{\mathbf{x}} + H_y \hat{\mathbf{y}} + H_z \hat{\mathbf{z}})$ is the magnetic field amplitude, \mathbf{k} is the wave vector, and ω is the angular frequency.

2.1.2 One-Dimensional Confinement

While Subsection 2.1.1 described electromagnetic propagation in an unbounded region, in practice it is important to understand how electromagnetic radiation can be *guided*. Consider a three-layer slab waveguide shown in Figure 2.1, where n_{core} , n_{uclad} and n_{lclad} are used to denote the refractive indices of the core guiding layer, the upper cladding layer and the lower cladding layer, respectively. The slab waveguide provides one-dimensional confinement of the electromagnetic radiation. That is, the wave is free to travel along the infinite direction of propagation z and along the infinite direction of x , while it is confined in the y -direction.

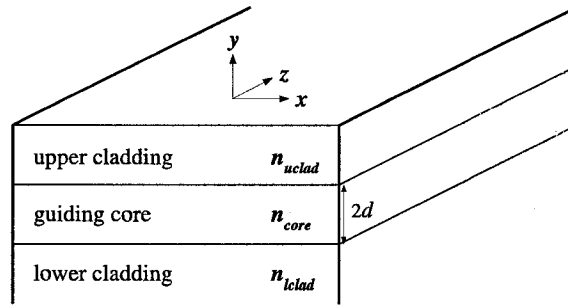


Figure 2.1: Slab waveguide structure.

When the electromagnetic wave is propagating along the $+z$ direction, equations (2.9) and (2.10) take the form:

$$\mathbf{E}(\mathbf{r}, t) = \mathbf{E}_0 e^{j(\omega t - \beta z)} \quad (2.11)$$

$$\mathbf{H}(\mathbf{r}, t) = \mathbf{H}_0 e^{j(\omega t - \beta z)} \quad (2.12)$$

where β is the z -component of the wave vector \mathbf{k} and is known as the *propagation constant*.

Because the slab structure is infinitely wide along the x -axis, both \mathbf{E} and \mathbf{H} are x -independent. Therefore, Maxwell's equations result in two distinct sets of linearly polarized solutions [20]:

1. Transverse electric (TE) solution – solution in which the electric field only exists perpendicular to the direction of propagation z . In this case $E_z = E_y = 0$, and

E_x satisfies:

$$\frac{d^2 E_x}{dy^2} + (n^2 k_0^2 - \beta^2) E_x = 0 \quad (2.13)$$

2. Transverse magnetic (TM) solution – solution in which the magnetic field only exists perpendicular to the direction of propagation z . In this case $H_z = H_y = 0$ and H_x satisfies:

$$\frac{d^2 H_x}{dy^2} + (n^2 k_0^2 - \beta^2) H_x = 0 \quad (2.14)$$

The profile of the various mode fields can now be derived by solving equations (2.13) and (2.14) for the three layers shown in Figure 2.1. The solution shows that the longitudinal fields must oscillate in the core guiding region, while they must decay in exponential fashion in the two cladding regions. The tails of the mode that propagate through the cladding regions are known as the *evanescent fields*.

An important parameter that is related to the propagation parameter β is the *effective index*, defined as:

$$n_{eff} = \frac{\beta}{k_0} \quad (2.15)$$

where k_0 is the free space vector, given as:

$$k_0 = \frac{2\pi}{\lambda_0} \quad (2.16)$$

where λ_0 is the wavelength in free space.

The effective index of the mode can be thought of as the index of refraction that governs the mode as it propagates along the z -direction. When a mode is guided, its effective index must satisfy:

$$\max(n_{uclad}, n_{lclad}) < n_{eff} < n_{core} \quad (2.17)$$

The value of the effective index for a given mode can be calculated by using the eigenvalue equation arising from the solution of the field profile equations and the corresponding boundary conditions. The normalized form of this equation for TE modes is given by [20]:

$$2V\sqrt{1-b} = m\pi + \tan^{-1} \sqrt{\frac{b}{1-b}} + \tan^{-1} \sqrt{\frac{b+\delta}{1-b}} \quad (2.18)$$

and for the TM modes:

$$2V\sqrt{1-b} = m\pi + \tan^{-1}\left(\frac{n_{core}^2}{n_{lclad}^2}\sqrt{\frac{b}{1-b}}\right) + \tan^{-1}\left(\frac{n_{core}^2}{n_{uclad}^2}\sqrt{\frac{b+\delta}{1-b}}\right) \quad (2.19)$$

where m is an integer, b is the normalized propagation parameter, δ is the asymmetry parameter of the waveguide, and V is the normalized frequency parameter, defined as:

$$b = \frac{n_{eff}^2 - n_{lclad}^2}{n_{core}^2 - n_{lclad}^2} \quad (2.20)$$

$$\delta = \frac{n_{lclad}^2 - n_{uclad}^2}{n_{core}^2 - n_{lclad}^2} \quad (2.21)$$

$$V = k_0d\sqrt{n_{core}^2 - n_{lclad}^2} \quad (2.22)$$

where d is half the thickness of the guiding core layer. It is important to realize that the only unknown in equations (2.18) and (2.19) is b , which is a function of n_{eff} . The integer term m is called the *mode number*. It can be shown that solutions to the eigenvalue equations (2.18) and (2.19) exist only for $m = 0, 1, \dots, m_{crit}$, and that for each allowed m there is only one solution. These solutions are the optical *modes* of the structure. Therefore, if the waveguide parameters are known, the effective index of a given mode can be obtained numerically from equation (2.18) for a TE mode or from equation (2.19) for a TM mode. Figure 2.2 shows the normalized b - V diagram for the first three TE modes for several values of the asymmetry parameter δ , where the curves are numerically derived from equation (2.18). Note that for a symmetric slab waveguide (i.e. $n_{uclad} = n_{lclad}$ and thus $\delta = 0$), there exists a solution for all values of V ; that is, there is always at least one mode that is guided in a symmetric slab waveguide. However, for an asymmetric slab waveguide, there exists a cut-off value for the normalized frequency, given by:

$$V_0 = \tan^{-1}\sqrt{\delta} \quad (2.23)$$

i.e. for $V < V_0$ the fundamental ($m = 0$) mode is not guided in the slab waveguide. In general, if the normalized frequency parameter V ranges over $V_m < V < V_{m+1}$, where:

$$V_m = V_0 + m\pi \quad (2.24)$$

then $m+1$ modes (TE_0, TE_1, \dots, TE_m) are supported. Curves similar to those shown in Figure 2.2 can also be numerically derived for the TM modes of a slab waveguide.

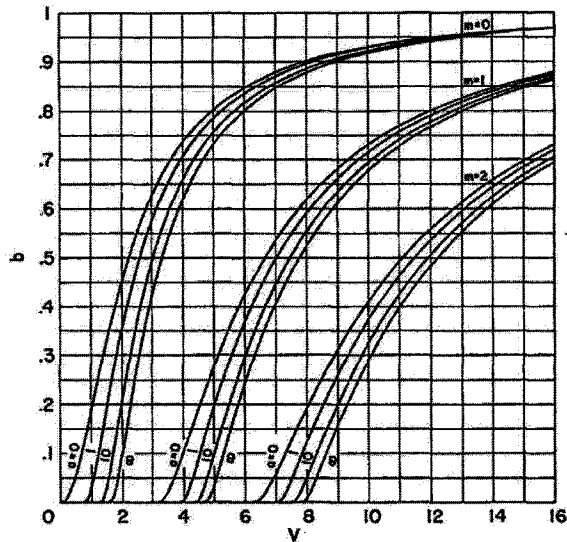


Figure 2.2: Normalized b - V diagram for the first three TE slab waveguide modes for several values of the asymmetry parameter. Taken from [22].

The analysis of the three-layer slab waveguide can be further extended to slab waveguides with multiple layers, such as the four-layer model of a silicon-on-insulator slab waveguide, as shown in Figure 2.3. An important difference between the SOI slab structure and the three-layer slab structure shown in Figure 2.1 is that SOI slab waveguides do not support lossless guided modes, since the thickness of the buried oxide layer is finite, and the same material is used for the guiding layer and the substrate of the slab waveguide. Thicker buried oxide layer will provide higher isolation and thus lead to lower optical losses.

2.1.3 Two-Dimensional Confinement

Most practical applications require confinement of light in two dimensions, such that an optical signal can be routed along a specified path. The additional horizontal confinement can be achieved using a rib waveguide structure as shown in Figure 2.4(a). It is important to note that strictly speaking the modes of a rib waveguide are not

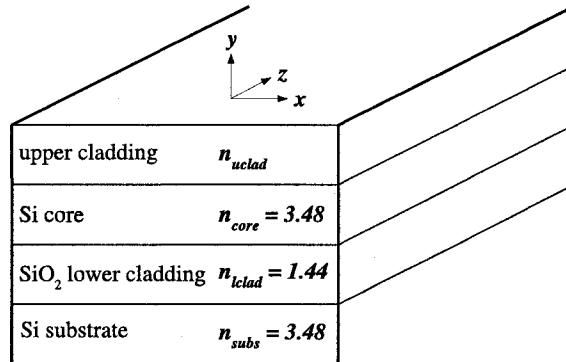


Figure 2.3: Silicon-on-insulator slab waveguide.

purely TE or TM modes, as is the case with a slab waveguide. The modes can be divided into two sets of hybrid modes: quasi-TE modes, for which all field components are assumed to exist except for E_z , and quasi-TM modes, for which all components are assumed to exist except for H_z .

An analytical solution to the two-dimensional wave equations of a rib waveguide is generally not possible due to the complexity of the boundary conditions. However, several techniques for numerical and semi-analytical solutions have been studied. The simplest semi-analytical approach is the effective index method (EIM), which obtains the approximate modes of a rib waveguide by treating the problem as four one-dimensional slab waveguide problems. The method divides the rib waveguide structure into three regions, as shown in Figure 2.4(b). To solve for the quasi-TE modes of the rib waveguide, first each of the regions is treated as an individual slab waveguide, resulting in the corresponding effective indices of the TE modes in each region. Second, the overall effective indices are found by solving for the TM solutions of a slab waveguide in a horizontal direction as shown in Figure 2.4(c), whose material refractive indices are replaced with the effective indices found in the first step. Note that in the second step the TM mode indices are being solved for to account for the rotated frame of reference [23]. Similar reasoning is used to find the quasi-TM modes of the rib waveguide.

Similarly to the slab waveguide, it is important to define the condition under which a rib waveguide is single mode (i.e. guides only the fundamental modes).

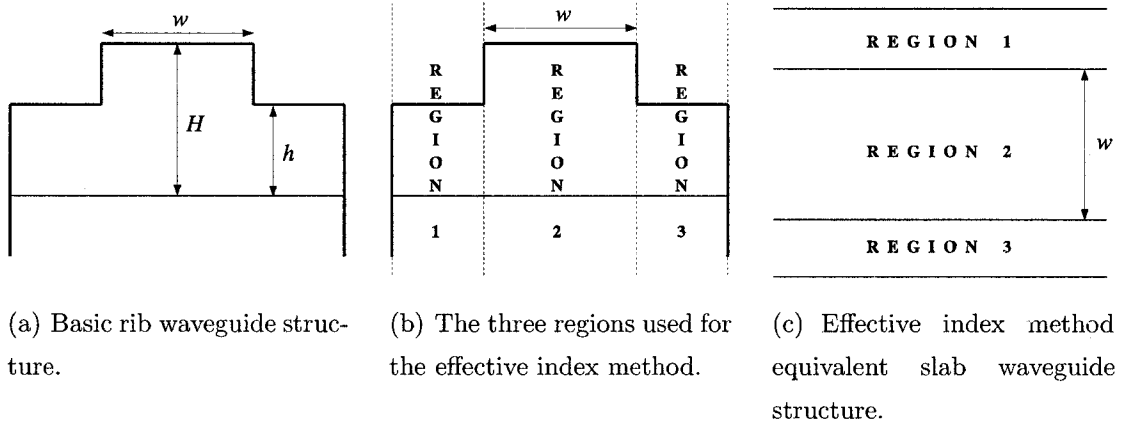


Figure 2.4: Rib waveguide analysis.

The effective index method and experimental evidence were used by a number of researchers ([24] [25] [26]) to predict that single-mode operation could be achieved if the waveguide dimensions were selected such that the following empirical relationship is obeyed:

$$\frac{w}{H} \leq \frac{r}{\sqrt{1-r^2}} - 0.05 \quad (2.25)$$

where r is the ratio between h and H , and the dimensions are defined in Figure 2.4(a).

The thickness of the buried oxide layer in a SOI rib waveguide must be sufficiently thick to prevent optical modes from penetrating the oxide layer and coupling into the silicon substrate. The required thickness will depend on the waveguide dimensions and on the optical mode, since each mode penetrates the cladding to a different depth. Figure 2.5 shows the required buried oxide layer thickness as a function of waveguide thickness such that the leakage losses to the substrate are below 0.001 dB/cm for the fundamental TE and TM modes at a wavelength of 1.55 μm .

2.2 Mach-Zehnder Interferometer

A Mach-Zehnder interferometer (MZI) is a well known structure that is widely used as the core mechanism for modulators, optical filters, switches, and other devices. The basic structure of a MZI is shown in Figure 2.6(a). The first junction splits the

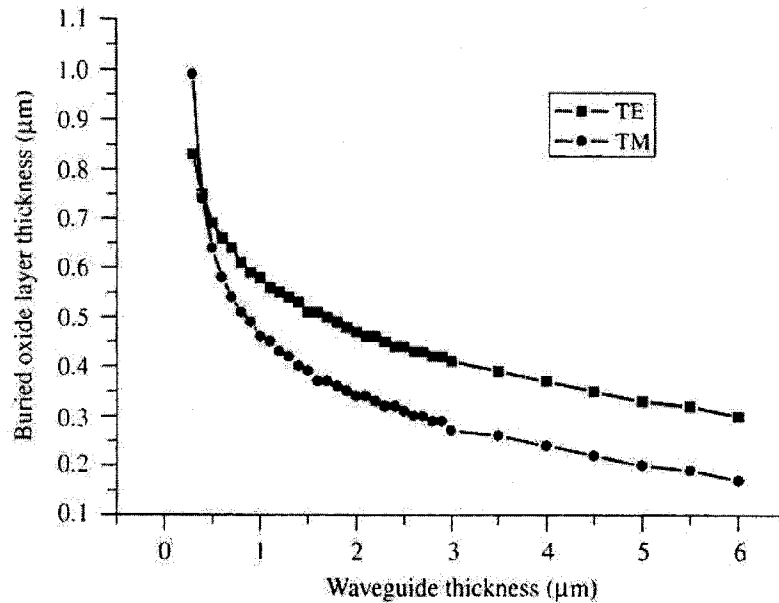


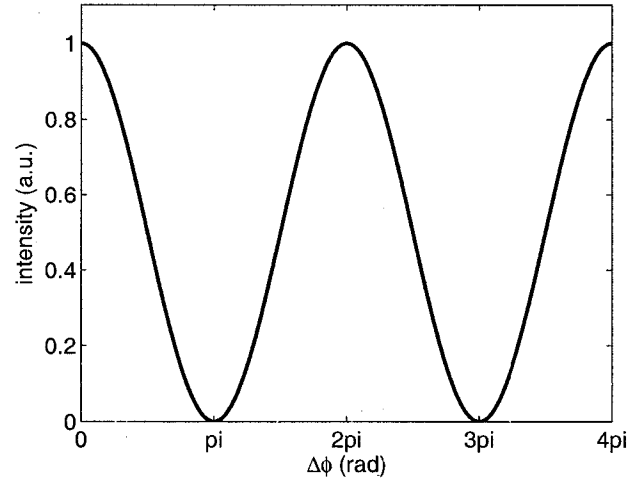
Figure 2.5: Buried oxide layer thickness versus silicon-on-insulator waveguide thickness for achieving leakage losses below 0.001 dB/cm for the fundamental TE and TM modes. Taken from [2].

input signal in two parts, and the resulting two signals take physically different paths, before recombining at the second junction. Depending on the difference between the optical path lengths in the two arms, the two parts of the signal may acquire different phase shifts, which causes the signals to interfere constructively or destructively at the second junction, producing a sinusoidal variation in the intensity of the output signal. In general, the two junctions need not be identical and can have different power splitting fractions, however in most practical applications the MZI is made using two identical 3-dB couplers or Y-splitters. When the two arms of the interferometer have nominally the same optical path length, the structure is known as a *balanced* MZI; otherwise an *unbalanced* MZI results.

The usefulness of the MZI in various applications is based on its ability to produce large changes in its output with small changes in the optical path length of one of its arms. The optical path can be changed by varying the physical length of one of the arms (e.g. by using a membrane that deforms under pressure variations [27]) or by changing the effective index in one of its arms (e.g. by changing the refractive index



(a) Balanced MZI structure.



(b) Normalized output intensity of a MZI as a function of phase difference.

Figure 2.6: Balanced Mach-Zehnder interferometer structure.

of the guiding layer [23] or the refractive index of the cladding [28]).

Assuming the first Y-junction splits the input signal E_{in} into two equal parts, the two signals in the arms of the interferometer are given by:

$$\mathbf{E}_{arm1} = \frac{\mathbf{E}_{in}}{\sqrt{2}} \quad (2.26)$$

$$\mathbf{E}_{arm2} = \frac{\mathbf{E}_{in}}{\sqrt{2}} \quad (2.27)$$

The two signals propagate along different paths, until reaching the second Y-junction. Let $\Delta\phi$ be the additional optical phase introduced in one of the interferometer arms. Thus just before the second Y-junction, the two signals have the

form:

$$\begin{aligned}\mathbf{E}_{arm1} &= \frac{\mathbf{E}_{in}}{\sqrt{2}} e^{j\omega t} \\ \mathbf{E}_{arm2} &= \frac{\mathbf{E}_{in}}{\sqrt{2}} e^{j(\omega t + \Delta\phi)}\end{aligned}\quad (2.28)$$

At the output, the two signals recombine to result in signal E_{out} , given by:

$$\begin{aligned}\mathbf{E}_{out} &= \mathbf{E}_{arm1} + \mathbf{E}_{arm2} \\ &= \frac{\mathbf{E}_{in}}{\sqrt{2}} (e^{j\omega t} + e^{j(\omega t + \Delta\phi)})\end{aligned}\quad (2.29)$$

Therefore, the time-averaged intensity of the output signal can be expressed as:

$$\begin{aligned}I_{out} &\propto \overline{\mathbf{E}_{out} \mathbf{E}_{out}^*} \\ &\propto \mathbf{E}_{in}^2 \cos^2 \left(\frac{\Delta\phi}{2} \right)\end{aligned}\quad (2.30)$$

where the horizontal bar denotes time-averaging.

Figure 2.6(b) shows the normalized intensity of the MZI output signal as a function of $\Delta\phi$, as described by equation (2.30). The maximum output amplitude occurs when the phase difference between the two arms of the interferometer is an integer multiple of 2π , while the minimum occurs when the phase difference satisfies $\Delta\phi = (1 + 2m)\pi$, where m is an integer. Moreover, the maximum slope and thus the maximum variation in the output signal intensity for a given change in $\Delta\phi$ occurs when $\Delta\phi = (1 + 2m)\frac{\pi}{2}$.

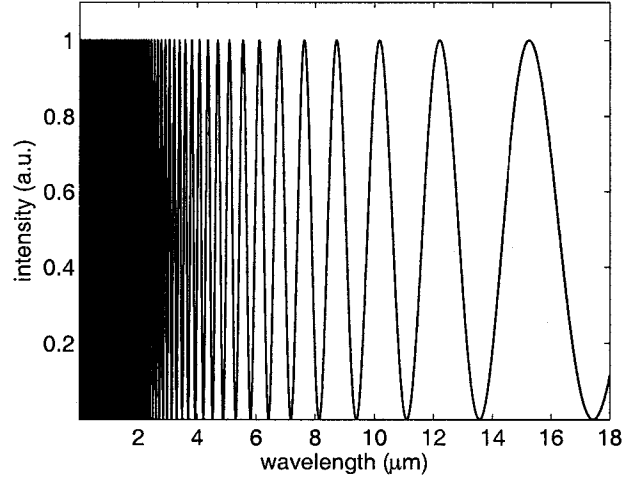
Note that for a perfectly balanced MZI, the output signal intensity will remain constant at its maximum value irrespective of the input signal wavelength. However, if even a slight imbalance is introduced into the structure, the phase difference between the two arms becomes wavelength dependent, which in turn causes the MZI output signal to be wavelength dependent. Figure 2.7(a) shows a MZI structure, in which the arms are designed to be of different physical lengths. The wavelength dependency of the output signal of such unbalanced MZI structure is shown in Figure 2.7(b).

Note also that the transmission spectrum as shown in Figure 2.7(b) can be used to approximate the physical path length difference between the two arms of an unbalanced MZI. The phase accumulated by a signal is given by:

$$\phi = \beta L = \frac{2\pi n_{eff}}{\lambda_0} L \quad (2.31)$$



(a) Unbalanced MZI structure.



(b) Normalized output intensity of an unbalanced MZI as a function of wavelength.

Figure 2.7: Unbalanced Mach-Zehnder interferometer structure.

Assuming that the propagation constants of the modes in the two arms are identical, the phase difference between the two signals at the second junction can be expressed as:

$$\Delta\phi = \beta(L_{arm1} - L_{arm2}) = \frac{2\pi n_{eff}}{\lambda_0} \Delta L \quad (2.32)$$

thus the change in $\Delta\phi$ with respect to change in wavelength can be expressed as:

$$\frac{\partial\Delta\phi}{\partial\lambda} = -\frac{2\pi n_{eff}\Delta L}{\lambda_0^2} \quad (2.33)$$

Now, when λ_0 changes enough to go from, e.g. one constructive interference peak to the neighboring one, the corresponding change in $\Delta\phi$ is 2π , and equation (2.33) takes the form:

$$\frac{2\pi}{\Delta\lambda} \approx \frac{2\pi n_{eff}\Delta L}{\lambda_0^2} \quad (2.34)$$

where $\Delta\lambda$ denotes the wavelength difference between two adjacent peaks. Finally, equation (2.34) can be rearranged to obtain:

$$\Delta L \approx \frac{\lambda_0^2}{n_{eff}\Delta\lambda} \quad (2.35)$$

i.e. for a given modulation spectrum of an unbalanced MZI (similar to one shown in Figure 2.7(b)), the actual path length difference can be estimated by measuring the horizontal difference between adjacent peaks and using equation (2.35).

A Mach-Zehnder interferometer can be used as an evanescent field sensor when phase difference between the two arms is induced by the measurand, which is introduced as the cladding material in one of the interferometer arms, known as the *sensing* arm. The second arm, the *reference* arm, is not exposed to the measurand, thus remaining in a constant reference state. The induced phase difference between the two signals causes them to interfere such that the output signal shows a sinusoidal variation that is directly related to the change in the refractive index of the measurand. In the case of the unbalanced MZI as shown in Figure 2.7, when the measurand changes the effective index of the mode in the sensing arm of the interferometer, the entire spectrum as shown in Figure 2.7(b) either compresses (in the case when $|\Delta\phi|$ decreases) or stretches (in the case when $|\Delta\phi|$ increases) relative to the wavelength axis. Note, however, that if the spectrum is observed over a short wavelength range, the effect of the stretch / compression appears as a nearly constant shift of the spectrum with respect to the wavelength axis. This shift (or the wavelength shift of one of the spectrum peaks [5]), can be used as an indication of the refractive index of the measurand.

Mach-Zehnder interferometer-based evanescent field sensors typically require single-mode operation. If several modes are propagating through the structure, a change in the measurand would affect the phase of each mode and may cause intermodal coupling. As a result, the intensity of the output signal can no longer be used as an indication of the refractive index of the measurand; instead, complex modal pattern image processing techniques are required [29].

A common difficulty in achieving high sensitivity with evanescent field sensing is that there is little interaction between the mode and the introduced measurand,

since only a very small portion of the mode's field travels as evanescent field in the cladding material. Thus to achieve significant cumulative effect, long interaction lengths are usually required. The device studied in this project explores an approach, where in order to increase the evanescent field *perforations* are introduced in the arms of the interferometer. The perforations cause larger portion of the wave field to travel through the cladding region, thus potentially increasing the evanescent wave sensitivity of the MZI-based sensor structure. The design of the perforations and their effect on the effective index of the propagating mode were studied mainly through simulation, and thus will be discussed in detail in Chapter 3.

2.3 Liquid Dynamics

The initial testing procedure for prototype refractive index sensors typically involves using water-based solutions. Since in this project the perforated region is the key element used for sensing, some characterization of liquid penetration into the perforations is provided.

The mathematical model presented here follows the analysis published in [30] (with background information taken from [31]), where a model is developed for the liquid uptake into porous particles during the process of iron sintering for the steel-making industry. Although the application is very different than the one in this project, the model describes liquid penetration rate into pores in general, and can at least be used to qualitatively explain the liquid behavior in the studied sensor structure.

In the case of an open pore, i.e. a pore which has two open ends as shown in Figure 2.8(a), as the liquid flows in, the replaced air is free to exit from the other end. However, if the pore has only one entrance (a closed pore) as shown in Figure 2.8(b), the air inside the pore cannot escape. This air will be compressed as liquid flows into the pore, thus slowing down the flow.

The rate of liquid flow into a closed pore is governed by two mechanisms: capillary-driven and diffusion-driven pore filling. The two processes occur simultaneously, however, at first, the capillary-driven mechanism dominates and causes rapid initial filling of the pore. This process slows down when an equilibrium between the capillary

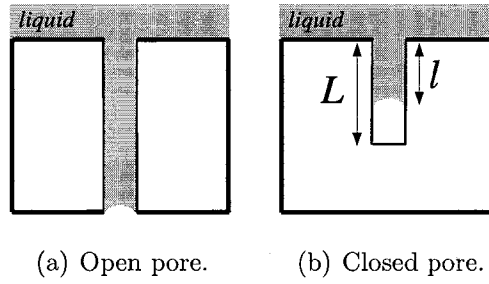


Figure 2.8: Examples of pore structures.

pressure generated by the fluid and the pressure of the air trapped by the fluid is reached. The pore filling process continues as a result of a much slower diffusion-driven mechanism, in which the trapped air slowly dissolves in the liquid and diffuses to the surface, eventually allowing the pores to become completely filled.

The switch in dominance between the two mechanisms occurs when l (defined as the length of the pore already filled with the liquid as shown in Figure 2.8(b)) is equal to l_{switch} , which is given by:

$$l_{switch} = L \left[1 + \frac{P_{atm} r^2}{2\gamma \cos(\theta) r - \frac{8\mu DRT}{H}} \right]^{-1} \quad (2.36)$$

where γ is the fluid surface tension, μ is the liquid viscosity, θ is the contact angle ($0^\circ \leq \theta < 90^\circ$), r is the radius of the pore, P_{atm} is the surrounding atmospheric pressure, D is the diffusivity of the gas (air) in the liquid, R is the ideal gas law constant, H is the Henry's law constant, T is the air temperature and L is the total length of the pore.

Thus for $0 \leq l < l_{switch}$, the pore filling time is governed by the capillary-driven process, which is given by:

$$t_{stage1} = \frac{8\mu}{A} \left[\frac{l^2}{2} + \left(\frac{B}{A} - L \right) l + \frac{B}{A} \left(\frac{B}{A} - L \right) \ln(B - Al) \right] \quad (2.37)$$

where $A = (2r\gamma \cos \theta + r^2 P_{atm})$ and $B = (2rL\gamma \cos \theta)$. Depending on the parameters of the pore and the liquid, l_{switch} may be smaller than L , i.e. portion of the pore remains unfilled when the capillary-driven process reaches equilibrium. At this time,

the second diffusion-driven mechanism becomes dominant, where the time it takes for the liquid to travel a distance l ($l_{switch} \leq l < L$) down a closed pore can be approximated by:

$$t_{stage2} = \frac{H}{2DRT}(l^2 - l_{switch}^2) \quad (2.38)$$

Therefore, the total time it takes for a liquid to fill a closed pore of length L is given by the sum of t_{stage1} and t_{stage2} . An example of the predicted time-dependency of the pore filling process is shown in Figure 2.9.

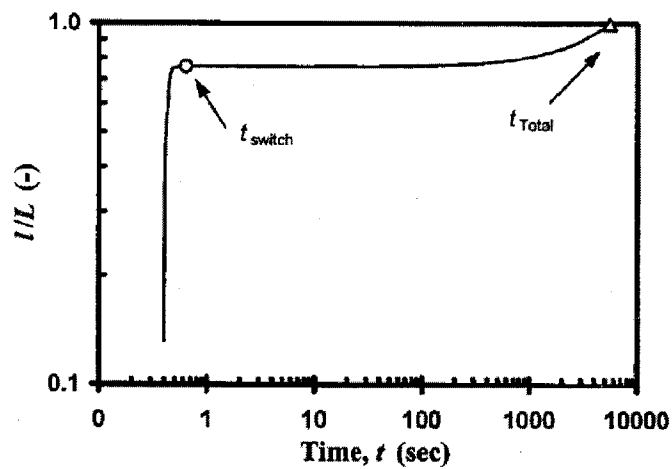


Figure 2.9: Example of the two-stage pore filling process for a 1 mm long, $0.455 \mu\text{m}$ radius pore filled with water. Taken from [30].

Note that experimental evidence described in [30] indicates that the presented model underestimates the time it takes for the pores to fully fill, and thus can only be used to predict qualitatively the effects of variations in the pore or liquid properties. The predictions of this model and experimental observations related to the closed pore-like perforations in this project will be further discussed in Chapter 5.

Chapter 3

Design and Simulation

This chapter presents the design process used to arrive at the dimensions of the perforated Mach-Zehnder interferometer structure, and the simulation work performed to model its optical behavior. Section 3.1 describes the chosen dimensions of the basic rib waveguide structure. In Section 3.2 the design of the perforated waveguide region is presented. This includes the design of the perforations themselves, and the analysis of their effect on the average effective index of the propagating mode and the power loss of the structure. Section 3.3 combines the mathematical model of a Mach-Zehnder interferometer with the simulated behavior of the perforated waveguide to model the expected optical behavior of the perforated Mach-Zehnder interferometer structure. In Section 3.4 a concise summary of the chosen device parameters and the simulation results is provided.

Unless otherwise stated, all simulations were done for an input wavelength of $1.55 \mu\text{m}$. Table 3.1 shows the materials used in the simulations and their corresponding refractive index values at $1.55 \mu\text{m}$ [32] [33].

3.1 Waveguide Structure

Due to financial considerations, an existing mask was used for the waveguide-based devices fabricated in this project (for details of the mask see Section 4.2). Therefore, the width of the waveguides was set at $5 \mu\text{m}$. Moreover, SOI material with 3.4

Material	Refractive index
silicon	$n_{Si} = 3.48$
silica	$n_{SiO_2} = 1.44$
air	$n_{air} = 1.00$
water	$n_{water} = 1.32$

Table 3.1: Refractive index values used in simulations ($\lambda_0 = 1.55 \mu\text{m}$).

μm thickness silicon film was used to fabricate the devices due to its availability in the Carleton microfabrication laboratory. As a result, in determining the waveguide dimensions for single-mode operation using the condition described in equation (2.25), the width of the waveguide (w) and the silicon film thickness (H) parameters were fixed. Although equation (2.25) is often quoted as the single-mode condition for a rib waveguide, it is important to note that it is a fit for a set of experimental results, and is not a sufficient condition for single-mode operation. Simulations using a mode solver for a given rib waveguide structure typically give a better indication on whether the structure supports any higher order modes.

Unfortunately, during the first stages of fabrication the thickness of the silicon film in the SOI material was mistakenly taken as $4 \mu\text{m}$ due to an incorrect label. With this thickness it was found that rib depth of $0.74 \mu\text{m}$ ($h = 3.26 \mu\text{m}$) satisfies equation (2.25), and mode solver simulations were used to confirm that the structure indeed forms a single-mode waveguide.

However, for a $3.4 \mu\text{m}$ thickness silicon film, a rib depth of $0.74 \mu\text{m}$ supports not only the fundamental TE and TM modes, but also the first order TM mode, as shown in Figure 3.1. The mode solver used to obtain the modes in Figure 3.1 is FIMMWAVE by Photon Design, which uses the Film Mode Matching (FMM) method [34]. FIMMWAVE mode solver results were confirmed with an equivalent simulation in FEMLAB, a finite element method (FEM) simulation program [35], however these results were not included here to avoid redundancy. The mistake was realized at a much later stage in the project, at which time an additional fabrication round was not possible because of unavailability of equipment and time limitations.

However, although the waveguide with the chosen dimensions supports a first

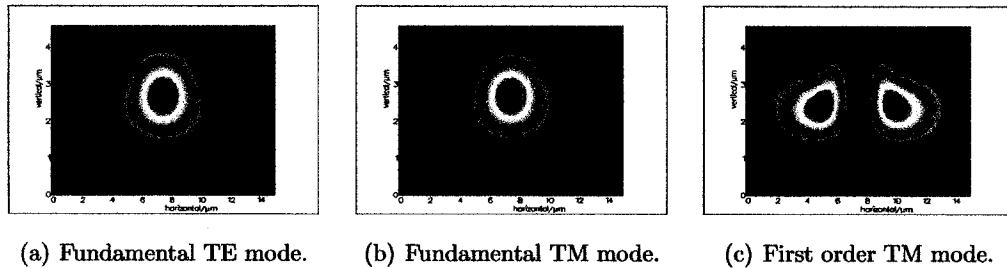


Figure 3.1: FIMMWAVE two-dimensional mode solver simulation results, showing the intensity distribution of the supported modes of the waveguide structure (input wavelength $\lambda_0 = 1.55 \mu\text{m}$).

order mode, with proper alignment the experimental setup that was used in the measurement stage of the project (described in detail in Chapter 5) does not easily excite higher order modes. This is due to the fact that the mode profile of the input fiber matches much more the fundamental waveguide mode, rather than any higher order modes. Yet, if the input fiber is not perfectly aligned to the center of the input waveguide, there is a possibility that the higher order mode will also be excited, or the optical signal will evolve into the higher order mode as it propagates through the interferometer structure. This issue will be discussed further in Section 3.3.

3.2 Waveguide Perforations

The perforated waveguide region is the key mechanism that is used to extend the evanescent field of the propagating mode in order to enhance the sensitivity of the sensor. In order to avoid any periodic effects, the perforations are placed in a random manner in the waveguide core, as illustrated in Figure 3.2(a). The random placement of the perforations also eases the fabrication process, as their exact placement is not critical.

Because the perforated waveguide structure varies in three-dimensions, a three-dimensional optical simulation setup was required. To ease the simulation setup, the perforations were placed in a pseudo-random pattern on a $1 \times 1 \mu\text{m}$ grid. In this initial

investigation of the perforated waveguide structure, no specific algorithm was used for the pseudo-random distribution. The placement of the perforations was generally configured such that they are uniformly distributed between the available positions on the $1 \times 1 \mu\text{m}$ grid. The basic building block of the grid that was used in the simulations is shown in Figure 3.2(b), and the block is repeated for longer lengths of the perforated waveguide.

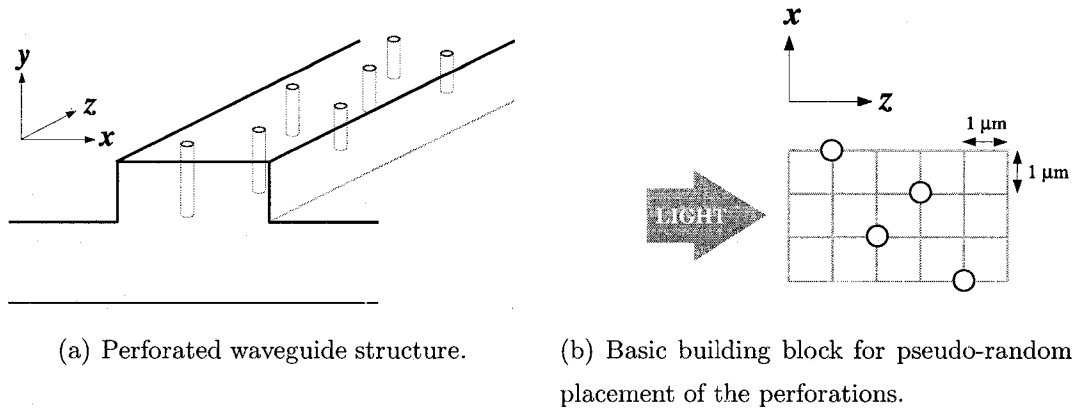


Figure 3.2: Simulation setup of the perforated waveguide.

The objective of the three-dimensional simulations of the perforated waveguide structure is to answer the following three questions:

1. What should the dimensions of the perforations be in order for the perforated region to enhance the sensitivity of the sensor? Subsection 3.2.1 discusses the relevant simulations and the chosen dimensions for the perforations.
2. What effect do the perforations have on the average propagation constant of the structure? Subsection 3.2.2 presents the simulations done to answer this question, and the results obtained.
3. What is the predicted power loss due to the light scattering as a result of the waveguide perforations? Subsection 3.2.3 describes the optical power simulations of the perforated waveguide structure.

Note that because three-dimensional optical simulations are very resource intensive and time consuming, the length of the perforated waveguides simulated is limited to $9\ \mu\text{m}$, consisting of two building blocks shown in Figure 3.2(b). As will be described in Chapter 4, the actual length of the perforated region was set at $100\ \mu\text{m}$, thus the obtained simulation results for the $9\ \mu\text{m}$ long structure are used to infer the effects of the perforations over a $100\ \mu\text{m}$ waveguide length.

The main optical simulation tool chosen to simulate the perforated waveguide structure was OptiFDTD, a finite-difference time-domain (FDTD) simulation package developed by Optiwave Systems Inc. The FDTD approach is based on a direct numerical solution of the time-dependent Maxwell's equations, and its model is set up without any pre-assumptions of field behavior [36]. The FDTD method was chosen because it does not use any assumptions and thus is able to simulate any structure, including three-dimensional small-scale structures like the perforated waveguide studied in this project. On the other hand, because FDTD solves the simulated problem by brute-force direct numerical solution, OptiFDTD simulations are extremely time consuming and resource intensive. Moreover, it proved to be a much more difficult task compared to other simulation tools to set up OptiFDTD simulations such that they converge to a valid solution.

In order to verify the validity of the simulation results obtained with OptiFDTD, an additional simulation tool, FIMMWAVE (and its three-dimensional extension module FIMMPROP) developed by Photon Design, was used. This software uses the eigenmode expansion algorithm, where the optical properties of a structure are fully characterized by the local modes of the structure and by coupling matrices between different local modes [34]. Since OptiFDTD and FIMMPROP use two completely different methods to model a three-dimensional structure and solve for its optical properties, if their results agree, then one can be reasonably confident that the simulations were set up correctly and the results are valid.

In addition to using two different simulation tools to model the behavior of the perforated waveguide, another precautionary step was taken to verify the simulation setup. A standard SOI waveguide (without any perforations) was simulated with both OptiFDTD and FIMMPROP using the same simulation setup as for the perforated

waveguides. Although a standard waveguide could be simulated using much simpler and less time consuming two-dimensional simulation methods, this structure was simulated in three-dimensions primarily as a sanity check for the simulation setup. A cross-check of the three-dimensional results with simpler and more stable two-dimensional simulation methods allowed a confirmation that the three-dimensional results are reasonable. Moreover, the standard waveguide structure was used as a reference for understanding the results obtained with a perforated waveguide, as will be further discussed in Subsection 3.2.2. It is important to note that for all three-dimensional simulations, grid convergence tests were performed to ensure that the simulation setup produces results that are consistent up to the sixth decimal digit of the calculated values.

Note also that the simulation work in this chapter and the experimental measurements in Chapter 5 concentrate only on the TM modes of the structure. While obtaining results for both the TE and the TM modes was not feasible in the given time frame due to long simulation times, the TM mode was chosen because, as was shown in [37], for most practical cases the TM mode is more sensitive to the refractive index variations of the upper cladding material than the TE mode.

3.2.1 Dimensions of the Perforations

The waveguide perforations act as a means to increase the interaction of the optical mode with the surrounding medium that acts as an upper cladding. In order to quantify the effects of the perforations, the *average effective index*, or equivalently the *average propagation constant*, of the mode that propagates through the structure is studied. That is, it is the effective index that the mode experiences on average while propagating through the perforated rib waveguide. Since the structure varies in three dimensions, no known simulation tool can provide the average effective index experienced by the mode. Therefore, the following approach to obtain it has been developed.

A mode propagates in an optical waveguide with a certain propagation constant β , defined as the phase delay per unit propagation distance. Equivalently, this can

be expressed as:

$$\beta = \frac{2\pi}{\lambda_m} \quad (3.1)$$

i.e. the wave accumulates 2π phase delay while traveling distance equivalent to its wavelength λ_m . As previously mentioned in equations (2.15) and (2.16), β is also defined as:

$$\beta = k_0 n_{eff} = \frac{2\pi}{\lambda_0} n_{eff} \quad (3.2)$$

where k_0 is the free space vector, n_{eff} is the effective index and λ_0 is the wavelength in free space. Combining equations (3.1) and (3.2), the following relationship is obtained:

$$n_{eff} = \frac{\lambda_0}{\lambda_m} \quad (3.3)$$

i.e. for a known free space wavelength λ_0 , if one can observe the wave pattern at a fixed time and measure the wavelength λ_m , equation (3.3) can be used to calculate the effective index of the propagating mode. Following the same logic, if one were to find the *average* λ_m then the *average* n_{eff} can be obtained.

Therefore, for all three-dimensional simulations, the electrical field oscillation pattern was analyzed using Fourier analysis to find the dominant frequency component. The inverse of the dominant frequency component represents the average wavelength of the mode, which is then used to calculate the average effective index of the mode using equation (3.3).

A number of factors controlled the placement and the profile of the perforations:

1. The perforations were placed in a pseudo-random manner on a $1 \times 1 \mu\text{m}$ grid as was previously shown in Figure 3.2(b). Note that because of very time and resource-consuming simulations, it was not possible to obtain an optimized value for every single parameter within the available time frame. It was therefore decided that the placement of the perforations on a $1 \times 1 \mu\text{m}$ grid will not be varied throughout the project.
2. The goal of the perforations is to increase the interaction between the mode field and the cladding material. However, the perforations also cause the undesired effect of light scattering. In order to avoid excessive light scattering,

the diameter of the perforations should be small, such that the perturbations that they create are much smaller than the wavelength of operation. Due to the restrictions of the fabrication process as will be described in Chapter 4, the smallest achievable diameter was found to be $0.3 \mu\text{m}$.

3. The depth of the perforations affects the profile of the mode. Deeper perforations cause greater sensitivity to the cladding material, while also causing larger power loss due to scattering of light. Keeping the placement of the perforations constant, the diameter set at $0.3 \mu\text{m}$ and the input wavelength set at $1.55 \mu\text{m}$, a number of simulations were done to study the effect of perforation depth on the optical characteristics of a $9 \mu\text{m}$ long waveguide. Figure 3.3 shows the average effective index of the propagating mode and the power remaining in the waveguide as functions of perforation depth. As can be seen from the figure, waveguides with deeper perforations have lower average effective index, indicating greater evanescent field and thus higher sensitivity to the cladding material. However, deeper perforations also cause greater scattering of light, thus a trade-off exists between the sensitivity of the guide and the resultant power loss, which in practice limits the length of the perforated region. As a compromise between these two factors, a perforation depth of $0.9 \mu\text{m}$ was chosen.

3.2.2 Average Propagation Constant

Two important questions were set during the simulation work in order to assess the feasibility of using the perforated waveguide for evanescent field sensing. First, do the perforations cause a larger fraction of the mode field to act as the evanescent field in the cladding material? And second, is the perforated waveguide more sensitive to changes in the refractive index of the cladding material than a standard waveguide? To answer these questions, four waveguide structures were studied using the three-dimensional simulations:

1. Standard waveguide with air cladding – this structure was used to verify the

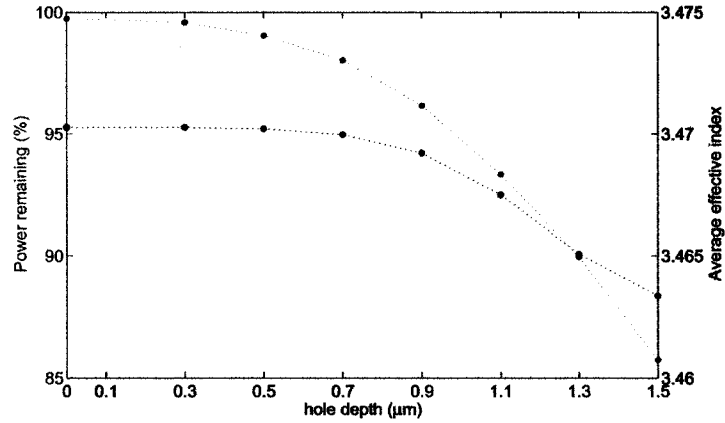
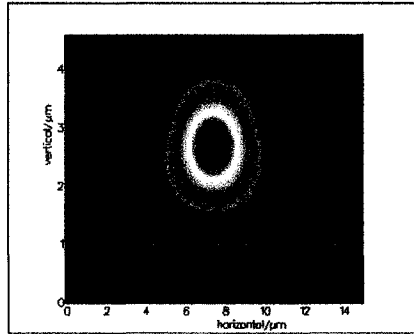


Figure 3.3: The effect of perforation depth on the average effective index of the fundamental TM mode and the optical power remaining at the end of a 9 μm long perforated waveguide.

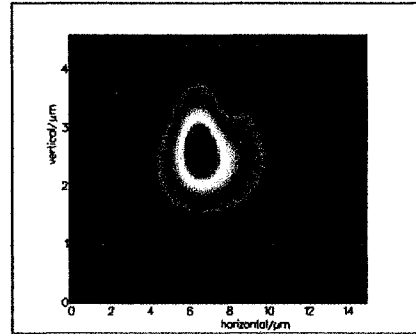
simulation setup, and to serve as a reference when studying the effects of perforations in case 2 below. The average effective index of a mode propagating through this waveguide is denoted as $n_{eff-std-wg-air}$.

2. Perforated waveguide with air cladding – this structure was used to study the effects of waveguide perforations on the propagation of an optical mode. The average effective index of a mode propagating through this waveguide is denoted as $n_{eff-perf-wg-air}$.
3. Standard waveguide with water cladding – this structure was used to study the effect of changing the cladding material of a standard waveguide from air to water on the propagation of an optical mode. The average effective index of a mode propagating through this waveguide is denoted as $n_{eff-std-wg-water}$.
4. Perforated waveguide with water cladding – this structure was used to study the effect of changing the cladding material of a perforated waveguide from air to water on the propagation of an optical mode. The average effective index of a mode propagating through this waveguide is denoted as $n_{eff-perf-wg-water}$.

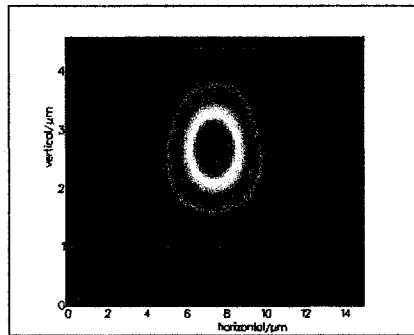
If the perforated waveguide structure is indeed successful in having greater evanescent field, the four relationships described in Table 3.2 between the average effective indices of the above four structures are expected.



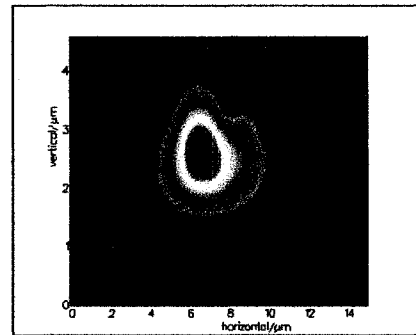
(a) Standard waveguide cross-section, air cladding ($n_{eff} = 3.470829$).



(b) Perforated waveguide cross-section along one of the holes, air cladding ($n_{eff} = 3.469631$).



(c) Standard waveguide cross-section, water cladding ($n_{eff} = 3.470856$).



(d) Perforated waveguide cross-section along one of the holes, water cladding ($n_{eff} = 3.469673$).

Figure 3.4: FIMMWAVE two-dimensional mode solver simulation results, showing the intensity distribution of the fundamental TM mode in selected waveguide cross-sections for air and water upper cladding (input wavelength $\lambda_0 = 1.55 \mu\text{m}$).

 Expected relationships and corresponding reasoning

$$n_{eff-std-wg-air} > n_{eff-perf-wg-air}$$

$$n_{eff-std-wg-water} > n_{eff-perf-wg-water}$$

The effective index of a mode that propagates through a standard waveguide can be obtained using a two-dimensional mode solver (see solution of the TM fundamental mode in Figure 3.4(a)). Since the waveguide profile remains constant along the propagation direction, the obtained effective index is also the average effective index of the mode ($n_{eff-std-wg-air}$).

For a perforated waveguide, however, the average effective index is a function of the effective indices of all the different cross-sections of the waveguide along the propagation direction – i.e. cross-sections along one of the holes (see Figure 3.4(b) for one solution) and cross-sections that do not intersect any holes (Figure 3.4(a)). Since the effective index of the case in (b) is lower than in (a) (i.e. in case (b) larger portion of the mode extends outside the silicon guiding layer), it can be concluded that the average effective index for a perforated waveguide ($n_{eff-perf-wg-air}$) must be smaller than the effective index for a standard waveguide ($n_{eff-std-wg-air}$).

The same reasoning can be used to explain the relationship between the average effective indices for the standard and the perforated waveguides with water cladding.

$$n_{eff-std-wg-air} < n_{eff-std-wg-water}$$

$$n_{eff-perf-wg-air} < n_{eff-perf-wg-water}$$

When the cladding material is changed from air to water the effective index of the mode is subjected to two effect: it tends to increase because the refractive index of the cladding is increased, and it tends to decrease because the mode becomes less confined to the silicon waveguide.

Two-dimensional mode solver simulations indicate that the former effect is dominant and thus the effective index increases when cladding material is changed from air to water (see Figure 3.4 part (c) versus (a), and (d) versus (b)). Therefore, the net effect for the average effective indices is that they also grow when the refractive index of the cladding is increased from $n_{air} = 1$ to $n_{water} = 1.32$.

Table 3.2: Expected relationships between the average effective indices for the four simulated waveguide structures.

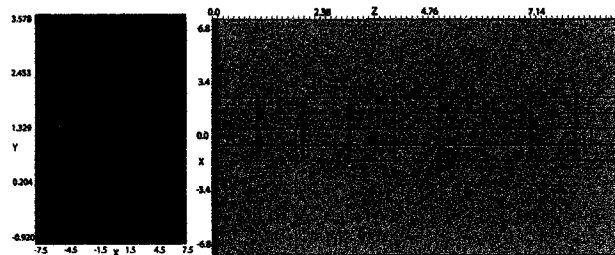
Parts (a) and (b) of Figure 3.5 show the setup used for the OptiFDTD simulations of a standard and a perforated waveguide (note that the figures are not drawn to scale). As previously mentioned, the waveguide lengths are limited to $9 \mu\text{m}$ due to long simulation times. In all cases, continuous wave excitation is used with $\lambda_0 = 1.55 \mu\text{m}$ as the input wave wavelength.

The last stage of the OptiFDTD simulation is a Discrete Fourier Transform (DFT) of the field propagation results, therefore the simulated data is stored in complex form. The magnitude of the propagated field for both the standard and the perforated waveguides is shown in Figure 3.5 parts (c) and (d), respectively. As expected in the standard waveguide case, no light scattering is evident as the mode propagates along the waveguide. In the perforated case, however, it can be clearly seen that the perforations cause light scattering into the surrounding regions.

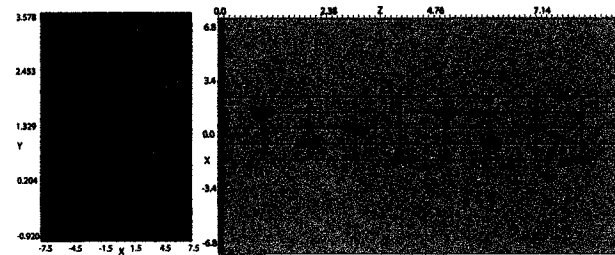
In order to obtain information about the wavelength λ_m of the light in the waveguide, it is necessary to observe the spatial periodic modulation of the wave, which can be done by displaying only the real or only the imaginary part of the simulated DFT results. Figure 3.5 parts (e) and (f) show the real part of the propagated field in the standard and the perforated waveguides. Fourier analysis of the periodic nature of the data in parts (e) and (f) were then used to find the wavelength λ_m of the wave, and the average effective index of each structure was obtained using equation (3.3). Table 3.3 summarizes the calculated average effective index results based on the OptiFDTD simulations.

Index	Value
$n_{eff-std-wg-air}$	3.470293
$n_{eff-perf-wg-air}$	3.469213
$n_{eff-std-wg-water}$	3.470322
$n_{eff-perf-wg-water}$	3.469361

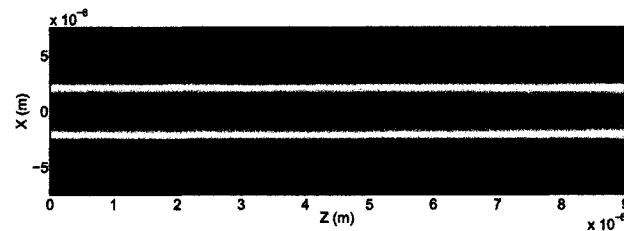
Table 3.3: Average effective index results based on OptiFDTD simulations.



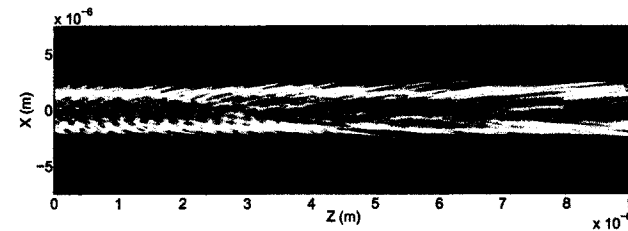
(a) Standard waveguide cross-section (red region represents silicon material) and top view.



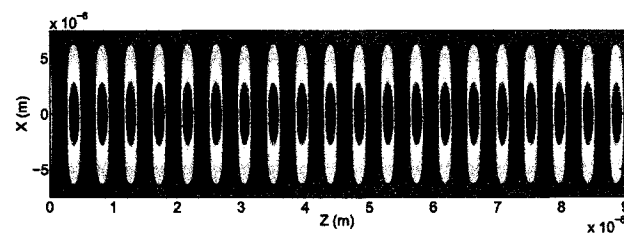
(b) Perforated waveguide cross-section along one of the holes (red region represents silicon material) and top view.



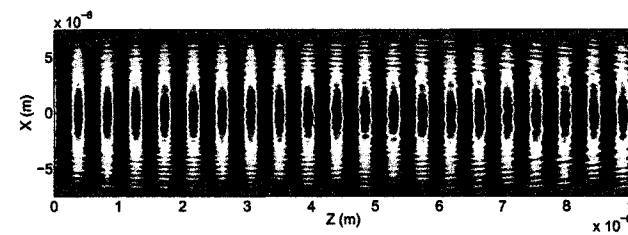
(c) Standard waveguide, magnitude of the DFT results.



(d) Perforated waveguide, magnitude of the DFT results.

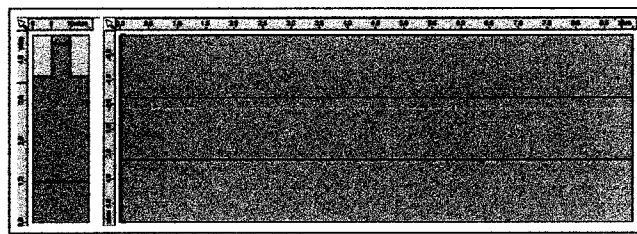


(e) Standard waveguide, real part of the DFT results.

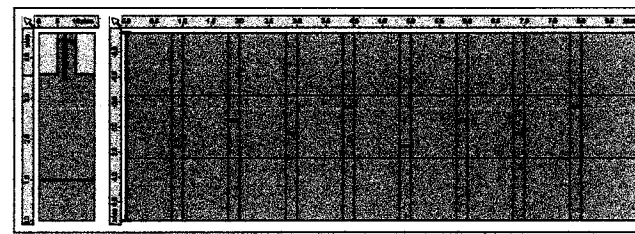


(f) Perforated waveguide, real part of the DFT results.

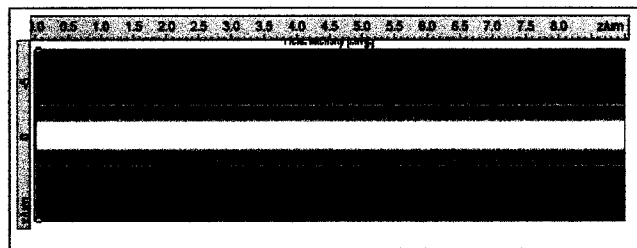
Figure 3.5: OptiFDTD three-dimensional simulation results for $9 \mu\text{m}$ long waveguide structures.



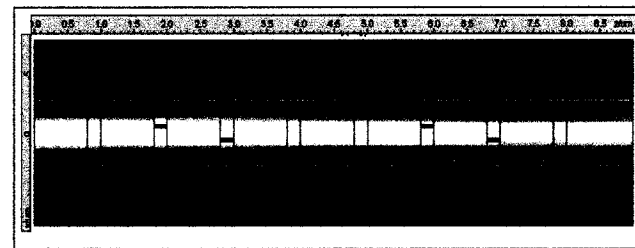
(a) Standard waveguide cross-section (red line superimposed to indicate the outline of silicon material) and top view.



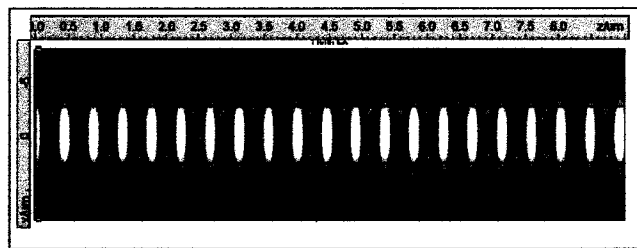
(b) Perforated waveguide cross-section along one of the holes (red line superimposed to indicate the outline of silicon material) and top view.



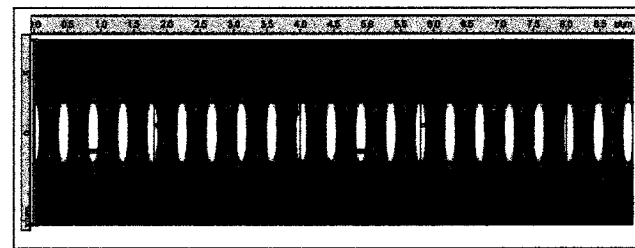
(c) Standard waveguide, time-averaged intensity results.



(d) Perforated waveguide, time-averaged intensity results.



(e) Standard waveguide, field amplitude results.



(f) Perforated waveguide, field amplitude results.

Figure 3.6: FIMMPROP three-dimensional simulation results for 9 μm long waveguide structures.

As a first check of the results, note that the four index values in Table 3.3 agree with the conditions outlined and explained in Table 3.2, which indicates that the results are at the very least sensible. As a second check, the question on whether the perforated structure is more sensitive to the variations in the cladding material than the standard waveguide should be addressed. Note that when the cladding material is changed from air to water, for the standard waveguide case the change in the average effective index is $\Delta n_{std} = 2.9 \times 10^{-5}$. The equivalent change for the perforated waveguide is $\Delta n_{perf} = 1.48 \times 10^{-4}$, i.e. ~ 5 times larger than the standard waveguide case. This indicates that based on the OptiFDTD results, the perforated structure is indeed more sensitive to variations in the cladding material than a standard waveguide with the same dimensions.

An equivalent simulation setup was created in FIMMPROP – Figure 3.6 parts (a) and (b) show the standard and the perforated waveguide structures (the figure is not drawn to scale). Note that because FIMMWAVE constructs its simulation model from rectangular geometries, the $0.3 \mu\text{m}$ diameter perforations were modeled as $0.2 \times 0.2 \mu\text{m}$ square perforations. As with OptiFDTD, the structures were limited to a length of $9 \mu\text{m}$, and the input wavelength was set to $\lambda_0 = 1.55 \mu\text{m}$.

The time-averaged intensities of the propagating fields are shown in parts (c) and (d) of Figure 3.6. In the perforated waveguide, the intensity diminishes after each encounter with a perforation, while in the standard waveguide case, the intensity remains constant, as expected. The periodic nature of the field amplitude, as shown in parts (e) and (f) of Figure 3.6, was analyzed using Fourier analysis to result in the average effective index values shown in Table 3.4. In this case, too, the four index values agree with the conditions outlined and explained in Table 3.2. Moreover, based on the FIMMPROP results, the perforated waveguide structure is ~ 8 times more sensitive to variations in the cladding material than a standard waveguide with the same dimensions.

Index	Value
$n_{eff-std-wg-air}$	3.471699
$n_{eff-perf-wg-air}$	3.465519
$n_{eff-std-wg-water}$	3.471736
$n_{eff-perf-wg-water}$	3.465820

Table 3.4: Average effective index results based on FIMMPROP simulations.

3.2.3 Optical Loss

An undesirable effect of the waveguide perforations is the scattering of the light as it hits the perforations. It is important to quantify this loss, as it can limit the length of the perforated region that can be used in practice.

To obtain information about the power loss due to the perforations in OptiFDTD, input overlap integral (IOI) calculations were used. The IOI computes the power overlap between the simulated results in a selected x - y plane and the input wave to the structure. As a sanity check it was verified that the standard waveguide case had nearly 100% of the power remaining at the end of the 9 μm structure. For the perforated waveguide, the percentage of power remaining at the end of the 9 μm with air cladding was found to be 94.8%. Based on this information, for a perforated waveguide of length 100 μm , 55.6% of power will remain in the waveguide, or equivalently, the perforations cause loss of ~ 2.6 dB. For water cladding, loss of ~ 2.52 dB is obtained (about 3.2% lower than air cladding).

In FIMMPROP, the power loss of a 9 μm perforated waveguide with air cladding was found to be 8.1%, which for a 100 μm long structure implies that 39.5% of the mode power remains in the waveguide (~ 4 dB loss). For a water cladding, the loss for a 100 μm long waveguide is ~ 3.8 dB, i.e. about 3.3% lower than with air cladding.

3.3 Mach-Zehnder Interferometer

The design of the Mach-Zehnder interferometer device was not a part of this project due to the availability of an existing mask that included waveguide and Mach-

Zehnder interferometer structures (more details on the mask are given in Section 4.2). This section describes the unbalanced Mach-Zehnder structure utilized for sensing in this project, and presents simulations related to insertion loss, modulation of the output signal and expected sensing behavior.

A schematic of the unbalanced MZI structure used in this project is shown in Figure 3.7. The geometrical dimensions of the structure are given in Table 3.5. Note that the length of the phase shifting region L is set to $100 \mu\text{m}$ for reasons that will be described in Section 4.2.

Parameter	Value
Splitter profile	cosine-bend
Splitter length A	8 mm
Splitter width B	$300 \mu\text{m}$
Interaction length L	$100 \mu\text{m}$

Table 3.5: Geometrical parameters of the unbalanced Mach-Zehnder interferometer.

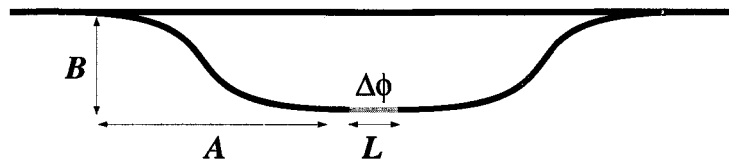


Figure 3.7: The unbalanced Mach-Zehnder interferometer structure used in this project.

OptiBPM, a beam propagation method simulation tool developed by Optiwave Inc. [38], was used to simulate the light propagation in the unbalanced MZI device, as shown in Figure 3.8. The simulation was set up in two-dimensions, where the effective indices of the core and the cladding regions were determined by the effective index method. Note that when the signals recombine at the second junction, the ripple in the output waveguide indicates that the undesirable second order mode that is supported by the waveguide may be excited. Although this is an undesirable effect that should not have happened if the waveguide depth was designed correctly, it does not invalidate the preceding analysis, since at the first junction the *fundamental*

modes of the split waveguides seem to be excited, as was assumed in the simulations described in Section 3.2, and the higher order mode is excited only at the output waveguide of the interferometer. OptiBPM models 4.2% loss as the mode propagates through the unbalanced MZI, within reasonable agreement with the $\sim 2.3\%$ insertion loss per power splitter as predicted in the original design of the mask [23].

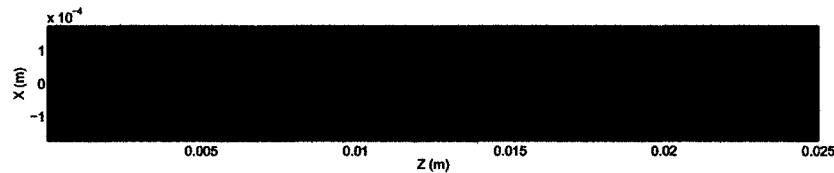


Figure 3.8: OptiBPM simulation of field propagation in the unbalanced Mach-Zehnder interferometer.

In order to observe the modulation of the output signal as a function of the input signal wavelength, a similar simulation setup was constructed in Apollo Photonic Solutions Suite (APSS) simulation package made by Apollo Inc. [39]. While the simulation setup is very similar to OptiBPM (two-dimensional beam propagation method simulation based on indices computed using the effective index method), APSS allows the computation of the relationship between the input and output modes at the device ports, which allows one to construct a normalized output intensity curve as a function of the input wavelength, as shown in Figure 3.9. From the spectrum shown in the figure, the physical path length difference between the two arms of the interferometer can be estimated using equation (2.35) to be $13.61 \mu\text{m}$.

In order to obtain a better estimate of the geometric path length difference between the two arms of the unbalanced MZI structure, the curvature profile of the interferometer power splitters was analyzed. The power splitter was designed using an S-bend cosine waveguide [23], which can be parameterized as [40]:

$$x(z) = x_s + A \left\{ 1 - \cos \left[\frac{2\pi}{P} (z - z_s) \right] \right\} \quad (3.4)$$

where x is the transverse coordinate, z is the coordinate along the axis of propagation, A is the amplitude, P is the period, and z_s and x_s are the coordinates of the bend starting position. A scan of the path defined by equation (3.4) using very small

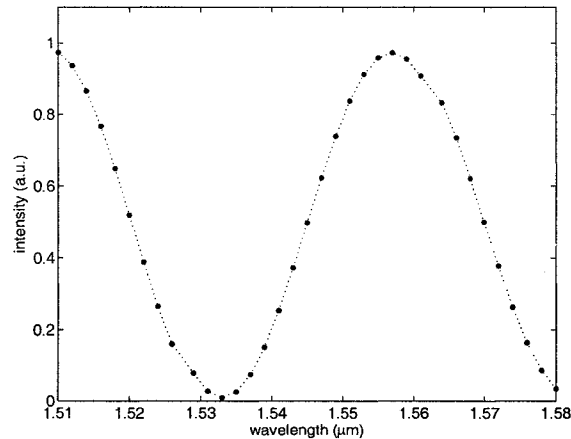


Figure 3.9: APSS simulation of output intensity as a function of input wavelength in the unbalanced Mach-Zehnder interferometer.

increments was used to obtain the length of the S-bend waveguide as 8.006935 mm, resulting in 13.87 μm total path length difference between the two arms of the interferometer (total length of the straight arm is exactly 17 mm, while the length of the curved arm is 17.01387 mm).

Apollo simulations can also be used to predict the behavior of the unbalanced MZI as a sensor device. However, its simulations are time consuming and the software is not very stable. Therefore, to obtain results in a more reasonable amount of time, MATLAB simulations based on the mathematical model of a MZI as derived in Section 2.2 were used instead.

The perforated waveguide region, as was shown in Figure 3.2(b), is the key sensing element in the investigated MZI-based sensor. The perforated area is created in both arms of the interferometer to keep the optical differences between the arms as small as possible. Recall from equation (2.30) that in order to obtain the normalized intensity of the output signal one needs to know the effective indices in the arms of the interferometer, which were calculated in Section 3.2, and the lengths of the two arms, which were found above. Figure 3.10(a) (red curve) shows the intensity spectrum obtained for the basic case when both arms of the perforated MZI have air cladding. The blue curve in the same figure shows the spectrum when the cladding material of the sensing arm (in this case the longer arm of the unbalanced interferometer) was replaced

by water, while the reference arm was left with air cladding. While Figure 3.10(a) is based on the average effective indices calculated by OptiFDTD, Figure 3.10(b) repeats the same exercise with the indices as calculated by FIMMPROP.

Note that strictly speaking, the curves plotted in Figure 3.10 are only valid at $\lambda = 1.55 \mu\text{m}$ because the average effective indices were simulated at this single wavelength. From equation (2.18) or Figure 2.2 it can be seen that n_{eff} is a function of λ , although since only a short wavelength range is used ($1.47 - 1.58 \mu\text{m}$) the value of n_{eff} will not vary by much. Nonetheless, for this reason the curves are drawn in solid line only around $1.55 \mu\text{m}$ and traced elsewhere to indicate that it is only an approximation.

Based on the plots in Figure 3.10, around $\lambda = 1.55 \mu\text{m}$ OptiFDTD predicts spectrum shift of 0.48 nm , equivalent to changing the phase difference between the two arms by 0.06 radians . FIMMPROP predicts a larger shift of 0.97 nm , equivalent to a change of 0.12 radians in phase difference.

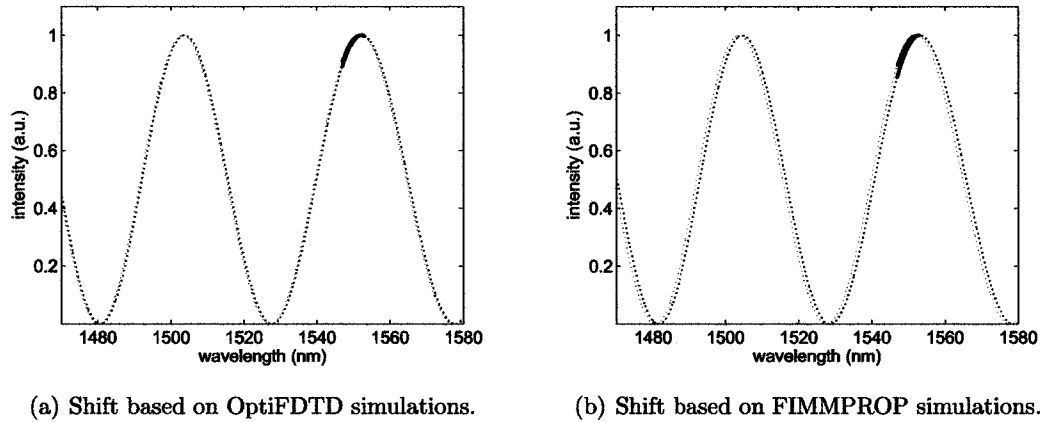


Figure 3.10: MATLAB simulation of the unbalanced Mach-Zehnder interferometer spectrum shift when measurand is changed from air (red curve) to water (blue curve).

3.4 Summary of Simulation Results

A number of simulations were performed to model the behavior of the perforated sensing region and the unbalanced Mach-Zehnder interferometer sensor structure as a whole. The results obtained are summarized in this section.

Figure 3.11 shows the summary of the critical dimensions for the perforated rib waveguide and the unbalanced MZI structure. The unbalanced MZI loss due to the two splitters was modeled to be 4.2% (~ 0.2 dB), while the optical loss due to the perforations for a $100 \mu\text{m}$ long waveguide region was predicted to be ~ 2.6 dB and ~ 4 dB by OptiFDTD and FIMMPROP, respectively. The physical path difference between the two arms of the interferometer was calculated by analyzing the profile of the splitters to be $13.87 \mu\text{m}$.

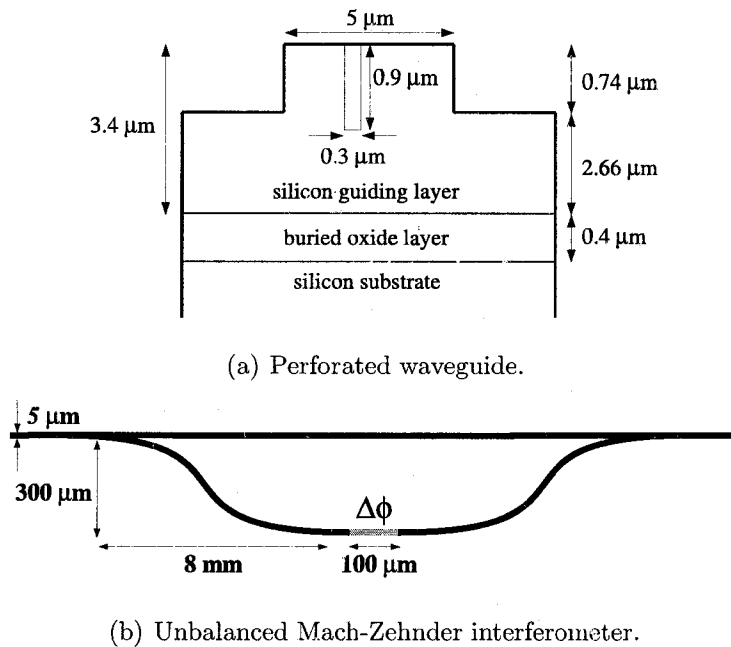


Figure 3.11: Summary of device dimensions.

The effect of the perforations on the average effective index of the optical mode was simulated by OptiFDTD and FIMMPROP, and the results obtained are summarized in Figure 3.12. Note that although the values obtained from the two simulation

programs are not identical, they are reasonably close. It is not realistic to expect simulation programs that use two different methods for modeling a three-dimensional device to provide identical quantitative results. The best one can hope for is for the two simulations to qualitatively predict the same device behavior, as is the case here.

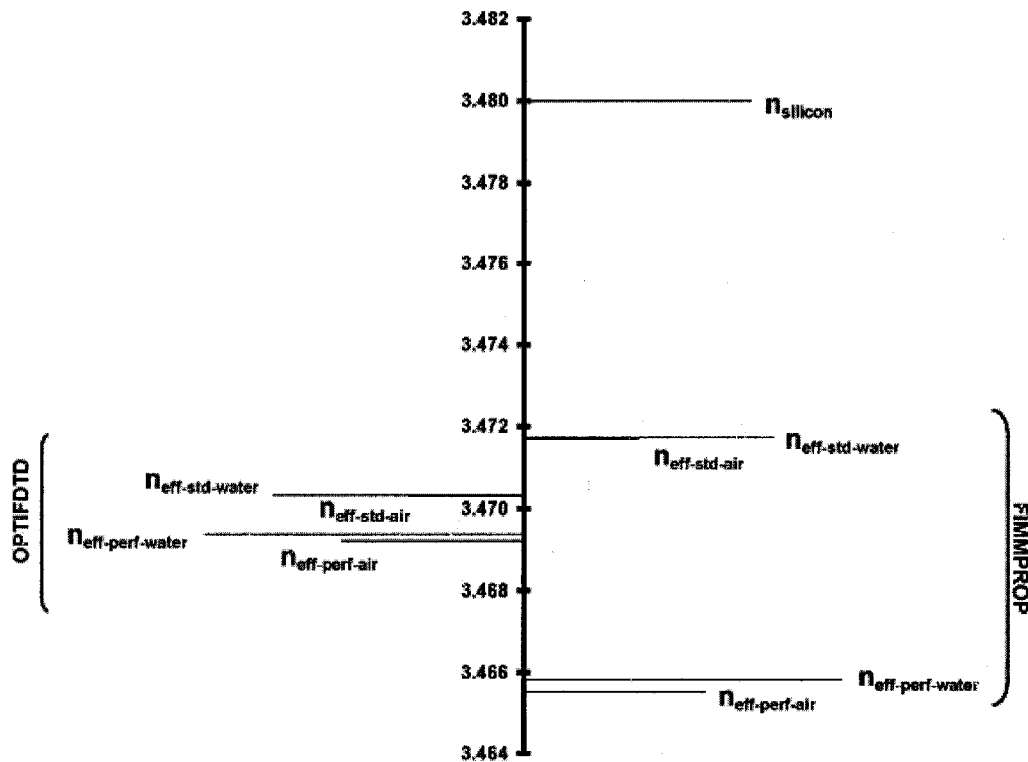


Figure 3.12: Summary of OptiFDTD and FIMMPROP average effective index simulation results.

Finally, the shift in the modulation spectrum of the MZI due to the sensing behavior of the device was modeled by combining the analytical model of a MZI and the simulation results obtained for the perforated waveguide structure. When the cladding of the sensing arm was changed from air to water, OptiFDTD simulations predicted a spectrum shift of 0.48 nm, while FIMMPROP predicted a shift of 0.97 nm.

Chapter 4

Fabrication

The perforated Mach-Zehnder interferometer sensor was realized using a combination of electron-beam and photo lithography processes. All fabrication was done in a Class 100 clean room at the Microelectronics Fabrication Facility at Carleton University.

In this chapter, the complete fabrication process is presented. Section 4.1 describes the materials used in the device fabrication. Section 4.2 outlines the main steps performed to fabricate the perforated MZI device, including the making of the perforated region, the fabrication of the interferometer structure, and the patterning of the sensing windows. In addition, the equipment used in the fabrication of the device is described, and issues related to fabrication quality are discussed.

4.1 Materials

Due to the relatively high cost of SOI wafers, initially standard p-type 10 Ω cm 100 mm silicon wafers were used to test the capabilities of the available fabrication equipment. Numerous experiments on the silicon test wafers enabled the establishment of the required fabrication parameters for the lithography and etch processes.

The actual sensor devices were fabricated on SOI wafers produced by the Smart-Cut process [41] by Soitec. The SmartCut process uses two standard silicon wafers to create a single SOI wafer. The first silicon wafer is thermally oxidized, and implanted

with high dose of hydrogen to weaken silicon lattice bonds at a given depth, while the second wafer is left untreated. The two wafers are bonded together at room temperature and subjected to thermal processing, which splits the implanted wafer along the peak of the hydrogen implantation profile and strengthens the bond between the two wafers. A fine chemical-mechanical polishing process is used to reduce the roughness of the resultant thin silicon film on top of the buried oxide layer. The process can be configured to obtain a wide range of silicon film and buried oxide thicknesses of high uniformity.

The SOI wafers used in the device fabrication have the nominal specifications shown in Table 4.1. Based on Figure 2.5, rib waveguide devices fabricated in these SOI wafers will have optical leakage losses below 0.001 dB/cm.

Specification	Value
silicon film thickness	3.4 μm
buried oxide thickness	0.4 μm
wafer thickness	500 μm
silicon film crystal orientation	(100)
silicon film resistivity	7 Ωcm

Table 4.1: Nominal specifications of the SOI SmartCut wafers used in device fabrication.

4.2 Fabrication Process

The complete runsheet for the fabrication of the perforated MZI sensor device is included in Appendix B. The main steps in the fabrication process are described next:

1. Electron-beam lithography to pattern perforations

In order to create the perforations in the SOI sample, a JSM-840 scanning electron microscope (SEM) made by JEOL [42] was adapted for electron-beam lithography and was used to write a pattern directly on a resist-coated wafer. To prepare the sample for electron-beam lithography, it was subjected to a

dehydration bake to eliminate adsorbed water, treated with the adhesion promoter hexamethyldisilazane (HMDS), and coated with a thin film of undiluted ZEP520A-7, a positive electron-beam resist produced by Zeon Corporation [43]. The spinning of the resist was typically done on an entire 100 mm wafer, since it produced a film of a more uniform thickness than smaller wafer sections. However, due to the relatively high cost of SOI, after the application of the resist the 100 mm wafer was cleaved into smaller pieces, typically into about 25×25 mm squares, which were used for the remainder of the fabrication process.

Figure 4.1 shows the designed pattern of pseudo-random perforations that was used as the input to the Nanometer Pattern Generation Software (NPGS), a control software for the scanning electron microscope. The total length of the pattern is $100 \mu\text{m}$, limited by the field of view of the SEM at the required magnification, and its width is $14 \mu\text{m}$, larger than the $5 \mu\text{m}$ width of the waveguides to account for translation errors of the SEM mechanical stage. The four lines above and below the perforations act as alignment marks when waveguides are exposed in a subsequent step.

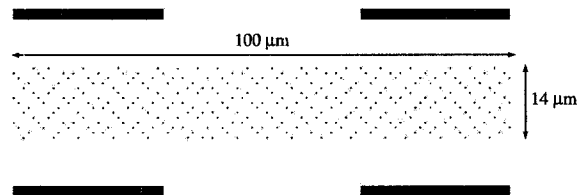


Figure 4.1: Perforations pattern designed for the SEM control software.

As much as possible, the written pattern was aligned to one of the $\{110\}$ planes of the SOI sample in order to facilitate a cleave that is perpendicular to the waveguides at a later stage. However, this goal was not always achieved due to the inability to see the sample edge at the writing magnification, as well as due to translation errors of the mechanical SEM stage. Table 4.2 shows the settings used for the SEM electron-beam lithography process.

After SEM write, the ZEP520A-7 resist was developed using *o*-xylene, followed by a rinse in isopropyl alcohol (IPA). Since resist development using wet

Setting	Value
magnification	900
acceleration voltage	39 kV
area dose	200 $\mu\text{C}/\text{cm}^2$
measured beam current	3 pA
coarse beam current	6 pA
emission current	100 μA
centre-to-centre spacing	97.4 \AA
line spacing	97.4 \AA
working distance	8 mm
tilt	0°
rotation	0°

Table 4.2: Electron-beam lithography SEM settings.

chemistry is likely to leave undesirable resist residue or scum on the uncovered areas, the sample was subjected to an oxygen plasma descum process using a Technics Planar Etch II plasma etcher. The oxygen plasma treatment is done for a short duration, such that any resist scum is removed, while the unactivated resist layers remain almost unaffected. For the perforations pattern the descum etch was done for 10 seconds with settings as shown in Table 4.3.

Setting	Value
Power	100 Watt
Gas	O ₂
Gas pressure	0.3 Torr
Base pressure	0.045 Torr

Table 4.3: Descum oxygen plasma process settings.

2. Perforations etch

The perforations were etched using electron cyclotron resonance (ECR) PlasmaTherm SLR-772 etcher system with SF₆/O₂ chemistry. Cryogenic ECR etching with fluorine based chemistries is an accepted technique for producing anisotropic and fast etching of silicon [44]. The sample is typically cooled

using helium gas, which is cooled externally by liquid nitrogen. Oxygen gas is added to enhance anisotropy through the creation of a thin layer of SiO_xF_y , which protects the sidewalls from being etched [45].

The PlasmaTherm SLR-772 system is designed to be used with 100 mm wafers. Therefore, for the etching steps, the SOI samples were temporarily attached to a 100 mm backing wafer using carbon adhesive tape. The carbon tape ensured that there is a good thermal contact between the sample and the backing wafer for proper sample cooling. Table 4.4 shows the ECR etcher settings used for the etching of the perforations.

Setting	Value
base pressure	1.6×10^{-6} Torr
gas pressure	6×10^{-3} Torr
temperature	-30° C
microwave frequency	2.45 GHz
microwave power	310 W
RF power	10 W
SF_6	3.65 sccm
O_2	2.21 sccm

Table 4.4: ECR etcher settings.

A number of experiments were performed in order to determine the smallest hole diameter achievable with the available equipment. Figure 4.2 shows a number of etched test patterns with different hole diameters. Below $0.3 \mu\text{m}$ diameter, the etched holes did not have vertical sidewalls, and displayed varying depths. Therefore it was concluded that with the available equipment, the smallest etched hole diameter is limited to $0.3 \mu\text{m}$. Note that to produce the $0.3 \mu\text{m}$ holes as shown in Figure 4.2(c), the SEM NPGS input file was designed with $0.2 \mu\text{m}$ diameter holes (see Figure 4.1). This disparity is likely due to undercutting of the resist mask. However, since this behavior was consistent for all etched perforations and reproducible across multiple experiments, in practice it did not present any significant problem.

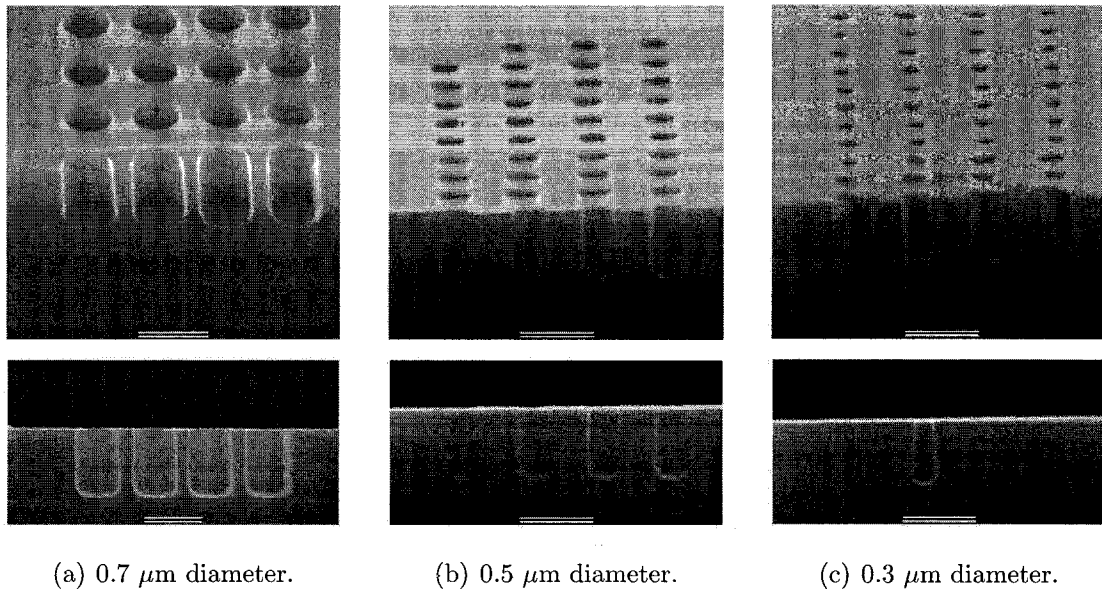


Figure 4.2: SEM pictures of etched perforation test structures (scale bars in all pictures correspond to $1 \mu\text{m}$).

As discussed in Section 3.2, the perforations should be much smaller than the wavelength of operation in order to avoid excessive power losses. Therefore, the final diameter of the perforations was set at $0.3 \mu\text{m}$, limited by the minimum diameter achievable with the available fabrication equipment. The depth was set at $0.9 \mu\text{m}$ based on simulations presented in Section 3.2. To achieve perforations of $0.3 \mu\text{m}$ diameter and depth of $0.9 \mu\text{m}$, the etching was done for 4.5 minutes.

To remove the sample from the backing wafer, both were soaked in acetone until the SOI sample could be easily lifted off the backing wafer. The resist and any remnants of carbon tape were then removed in Caro's acid.

3. UV lithography to pattern waveguide-based devices

MCMaster-CARLETON-OPTENIA-VOA1 mask, originally designed by P. Waldron as part of a joint research project between McMaster University, Optenia Corporation and Carleton University, was used in this project to pattern the waveguide-based devices. The portion of the mask that is relevant to this project is reproduced in Figure 4.3. As can be seen from the figure, the

mask contains straight waveguides, unbalanced Mach-Zehnder interferometers and balanced Mach-Zehnder interferometer structures. In the following sections of this report, the mask shown in Figure 4.3 is referred to as the 'waveguide-structures mask', to distinguish from the 'sensing-windows mask' that will be described in step 6. Table 4.5 shows the physical dimensions of the devices on the mask.

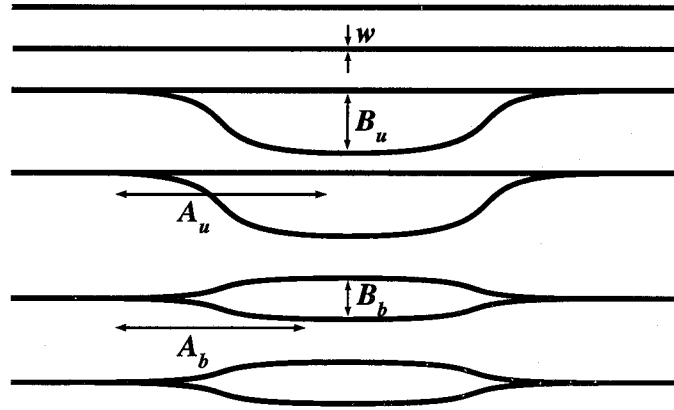


Figure 4.3: Layout of the waveguide-structures mask.

Dimension	Value
waveguide width w	$5 \mu\text{m}$
unbalanced MZI splitting length A_u	8 mm
unbalanced MZI distance between arms B_u	$300 \mu\text{m}$
balanced MZI splitting length A_b	7 mm
balanced MZI distance between arms B_b	$200 \mu\text{m}$

Table 4.5: Dimensions of the devices on the waveguide-structures mask.

To pattern the waveguide and interferometer devices on the SOI samples, a UV lithography process was followed. The sample was again subjected to a dehydration bake, treated with HMDS, and coated with a thin film of MICROPOSIT S1811, a positive photoresist optimized for g-line (436 nm) exposure produced by Shipley [46].

The photoresist-covered sample was exposed using a Karl Suss MA6 hard-

contact manual mask aligner system [47]. For this photolithography step, the mask must be aligned along the perforated regions on the SOI sample. However, due to the small size of the perforations, it is impossible to resolve them on the aligner system microscope. Therefore, special alignment marks were patterned along with the perforations (see Figure 4.1). While they are sufficiently far from the perforated regions to have no effect on the optical behavior of the waveguides, they are close enough to act as guidelines for the alignment of the waveguide-structures mask.

The SOI sample was exposed to UV light for 15 seconds with mask aligner settings as shown in Table 4.6.

Setting	Value
UV light source	mercury vapor arc lamp
exposure light wavelength	436 nm (g-line of the mercury spectrum)
lamp intensity	16 mW/cm ²

Table 4.6: Mask aligner settings.

After UV exposure, the S1811 photoresist was developed using MICROP-OSIT MF321 developer by Shipley [46], followed by a de-ionized water rinse and a post-bake to harden the inactivated photoresist. In order to ensure full removal of photoresist from uncovered areas, a 10 second descum process using a Technics Planar Etch II plasma etcher with oxygen chemistry was used once again (etcher settings shown in Table 4.3).

4. Waveguide devices etch

The waveguides-based devices were etched using electron cyclotron resonance (ECR) PlasmaTherm SLR-772 etcher system with SF₆/O₂ chemistry, similar to the process described in step 2. Figure 4.4 shows SEM pictures of a test waveguide etched in the ECR etcher, illustrating typical characteristics of the etch patterns. As can be seen from the figure, the waveguide demonstrates vertical sidewalls and thus highly anisotropic etching. The noticeable

surface and waveguide side-wall roughness is typical for patterns etched using dry reactive ion etching process. This roughness causes scattering of light, thus increasing the propagation losses of the waveguide-based devices. This issue will be discussed further in Section 5.2.

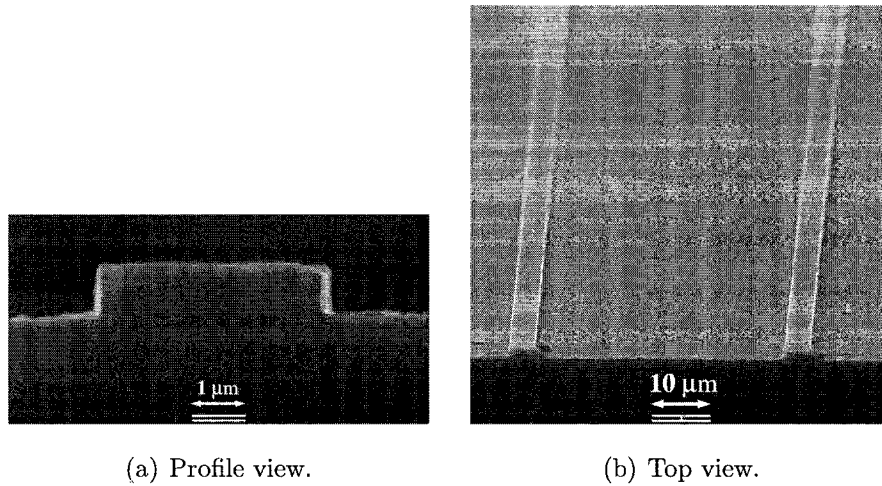


Figure 4.4: SEM pictures of a fabricated rib waveguide.

To perform the waveguide etch, the SOI sample was temporarily attached to a 100 mm backing wafer using carbon adhesive tape, and etched in the ECR etcher system for 2.4 minutes with settings as shown in Table 4.4 to produce $0.74 \mu\text{m}$ deep rib waveguide structures. Acetone was used to soak the wafer to break the adhesive in the carbon tape and remove the SOI sample, followed by a Caro's acid treatment to strip the remaining photoresist.

Figure 4.5 shows an SEM picture of a waveguide with pseudo-random perforations along its length. Note that since the perforations pattern was fabricated to be wider than the waveguide width (see Figure 4.1) to account for the translation errors of the SEM stage, there are perforations not only in the rib of the waveguide, but also on both sides of the rib (a number of such perforations can be seen on the left side of Figure 4.5). However, since the optical mode is tightly confined to the rib waveguide, these perforations are expected to have minimal effect on the optical characteristics of the guide.

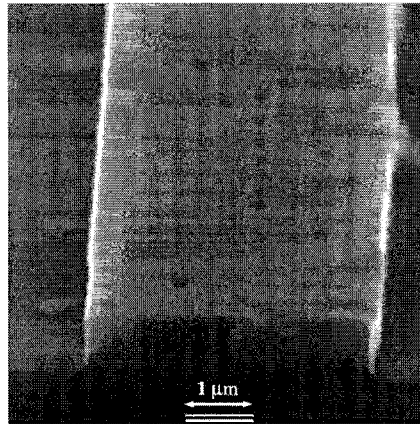


Figure 4.5: SEM picture of a fabricated perforated rib waveguide.

5. Thinning and cleaving of the sample

Efficient coupling of light from an optical fiber to a waveguide and vice versa is an important problem in any practical system that utilizes planar waveguide optics. High coupling efficiency is difficult to achieve because of a large mismatch in the mode size between an SOI waveguide and an optical fiber. Moreover, coupling is particularly problematic in semiconductors, since the refractive index of the silica fiber is very different from that of e.g. an SOI waveguide. Since light coupling efficiency is a major challenge that may limit practical application of planar waveguide-based optics, a number of advanced coupling structures have been researched and demonstrated in practice. One of the most popular methods of coupling light between an optical fiber and a waveguide has been a three-dimensional taper from the fiber dimensions to the waveguide dimensions in SOI [48]. Another technique involves using an inverted taper, where the taper decreases in size towards the optical fiber, thus the mode becoming less confined and more matched to the mode of the fiber [49]. Alternative coupler structures use an inverted prism to couple light into the waveguide [50] or utilize grating-assisted optical couplers [51].

While the above techniques have been demonstrated in practice with relatively high coupling efficiencies, they require fabrication of advanced coupling

structures. The simplest technique that can be used to couple light from an optical fiber to a waveguide is butt-coupling, where the optical fiber and the waveguide are brought end-to-end in close proximity. Therefore, the mode field of the transmitting device falls onto the end-face of the second device, which captures some of the transmitted light. Although this method introduces significantly larger optical losses compared to more advanced coupling techniques, it has the simplest setup and does not require fabrication of additional coupling structures. The butt-coupling technique was used to couple light into the waveguide-based devices during optical testing of the completed samples.

When a light beam is incident on the end-face of an optical waveguide, the efficiency with which the light is coupled into the waveguide is a function of three major factors [2]:

- (a) Overlap of excitation and waveguide fields – the large dimension mismatch between a typical waveguide (height / width $\sim 1\text{--}5\ \mu\text{m}$) and a single-mode optical fiber (core diameter $\sim 8\ \mu\text{m}$) create a significant mismatch between the excitation and the waveguide modes. To reduce the power loss due to modal mismatch, the devices on the waveguide-structures mask have tapered input and output waveguides, starting from a waveguide width of $15\ \mu\text{m}$ and gradually narrowing to the designed width of $5\ \mu\text{m}$. However, because the sample was cleaved, the input and output waveguides have been trimmed, resulting in tapers that start from smaller widths.
- (b) Reflections from the waveguide facets – reflections of light at air / silicon interfaces at the input and output facets of the waveguide can cause significant power loss. At normal or near-normal incidence, the power reflectivity can be approximated by:

$$R = \left| \frac{n_{air} - n_{Si}}{n_{air} + n_{Si}} \right|^2 \quad (4.1)$$

Assuming $n_{air} = 1$ and $n_{Si} = 3.48$, the reflection is about 31%, which is equivalent to 1.6 dB power loss at each facet. The loss due to facet reflections can be reduced by using an anti-reflection coating between the fiber

and the waveguide. The anti-reflection coating thickness is designed such that it is equal to quarter of the light wavelength, resulting in destructive interference of waves that are reflected from the front of the coating and the facet itself, thus reducing the reflection. No anti-reflection coating was used in this project since equipment and processes to produce it were not available.

- (c) Quality of the waveguide facet – rough waveguide end-faces introduce optical scattering, which further increases power loss when light is coupled into or out of the waveguide. Three main techniques exist for obtaining a smooth facet to minimize optical scattering: cleaving, end-face polishing and etching. In this project, a cleaving process was used to obtain sufficiently smooth facets, which is described in detail below.

In order to be able to cleave the sample along one of the $\{110\}$ planes, it was found necessary to thin the SOI wafer to a thickness of about $250 \mu\text{m}$. The sample was attached to a metal block using Crystalbond 509 mounting adhesive made by Aremco Products Inc. [52] by heating the metal block to a temperature of about 90°C , melting a small amount of the adhesive on the metal surface, placing the sample on the melted adhesive, and cooling the metal block to room temperature. The silicon substrate of the SOI sample was thinned from the initial wafer thickness of $\sim 500 \mu\text{m}$ to a final wafer thickness of $\sim 250 \mu\text{m}$ using an EcoMet III Grinder / Polisher made by Buehler [53] with settings as shown in Table 4.7.

Setting	Value
motor speed	200 rpm (0.4 DC mA on speed meter)
metal block mass	1.85 kg
sand paper	220 grit silicon carbide
grinding time	20 minutes
water flow	maximum

Table 4.7: Grinding wheel settings.

It was found that the sand paper is efficient at grinding silicon for only the first 10 minutes (presumably after this time the paper becomes clogged with debris). Therefore, a new 220 grit sand paper was used at the start of the grind, and it was replaced once again after 10 minutes. In addition, since the metal block used is significantly larger than the sample being ground, in order to avoid wobbling of the block and thus uneven grinding of the silicon substrate, a few sacrificial pieces of standard silicon wafer were also mounted on the block. The sacrificial silicon pieces were used to monitor the remaining thickness using a micrometer with 10 μm resolution.

The thinned sample was removed from the metal block by reheating the block until the adhesive liquified, and gently sliding the sample off. To remove the adhesive from the device surface, the sample was soaked for a few minutes in acetone, followed by Caro's acid treatment to ensure no adhesive remnants were present in the perforations.

As mentioned in Table 4.1, the crystal orientation of the silicon film in the SOI wafers used for device fabrication is (100). For (100) wafers there are two sets of {110} planes that intersect the surface, which can be used to obtain very clean cleaves. In order to cleave the sample, a diamond tipped scribe was used to make a small scribe along one of the {110} planes. Pressure was then applied precisely at the scribe until a crack along a {110} plane formed, creating a smooth cleave at the input / output edge of the sample.

6. UV lithography to pattern sensing windows

In order for the MZI to act as a sensor, only one of the interferometer arms must be exposed to the measurand. Therefore, an additional upper cladding layer has to be used to define 'sensing windows', i.e. to create a structure that exposes only the necessary regions, while protecting the rest of the sample. In order to create the sensing windows, a dark-field mask was created on a high-resolution silver halide emulsion photographic plate using a David Mann 1600A pattern generator and a Jade 4M-10AXYL step-and-repeat camera. Figure 4.6

shows the sensing-windows mask overlaid on top of the waveguide-based devices fabricated in steps 3 and 4 – the shaded regions represent the dark areas of the mask, while the unshaded windows are the transparent mask areas.

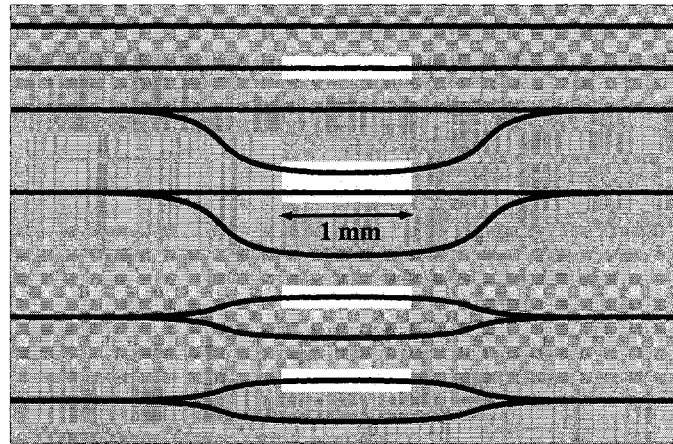


Figure 4.6: Layout of the sensing-windows mask.

S1811 photoresist was chosen as the material to be used for the sensing windows structure due to its availability in Carleton fabrication facilities, ease of removal and prior experience in using it for standard UV lithography. Experiments with S1811-covered samples in de-ionized water have shown that the photoresist's adhesion to silicon is sufficiently strong to protect selected regions from water-based solutions.

To pattern the sensing windows, UV lithography process was followed. After a dehydration bake, the sample was coated with a thin film of MICROPOSIT S1811 and exposed using a Karl Suss MA6 hard-contact manual mask aligner system [47]. The mask was aligned such that the windows expose the perforated waveguide regions on the SOI sample. The sample was exposed to UV light for 20 seconds with mask aligner settings as shown in Table 4.6.

After UV exposure, the S1811 photoresist was developed using MICROPOSIT MF321 developer by Shipley [46], followed by a de-ionized water rinse and a post-bake to harden the inactivated photoresist. In order to ensure that no photoresist residue is left in the exposed windows or in the waveguide per-

forations, an extended descum step using the Planar Etch II plasma etcher was performed with settings as shown in Table 4.3. A Nanometrics Nanospec AFT measurement system [54] was used to determine that the original thickness of the S1811 film is about $1.4 \mu\text{m}$, and the etch rate is approximately $0.138 \mu\text{m}/\text{minute}$. Therefore, a 3 minute long oxygen plasma etch was used to remove $\sim 0.4 \mu\text{m}$ of photoresist, leaving $\sim 1 \mu\text{m}$ thick protective layer in the covered regions, while eliminating any photoresist residues that may be present in the exposed windows or in the perforations.

Note that although S1811 completely covers the reference arm of the interferometer, it is expected that a negligible amount of photoresist gets inside the perforations due to liquid penetration behavior as described in Section 2.3. It is also worth noting that while a clean silicon surface is hydrophobic, silicon oxides are hydrophilic (typical contact angles for native silicon oxides range between 0° [55] and 43° [56]). Since the last two fabrication steps that the exposed regions of the device undergo are Caro's acid treatment and oxygen plasma, the exposed silicon is expected to have a thin layer of native oxide. This makes the exposed surface and perforations in the sample hydrophilic and thus more readily wetted by water or other solutions.

Chapter 5

Experimental Results

This chapter presents optical test results for the perforated unbalanced Mach-Zehnder interferometer sensor devices, which were fabricated based on the parameters identified in Chapter 3 and the process outlined in Chapter 4. Section 5.1 describes the measurement setup used for optical characterization of the devices. In Section 5.2 the measurements of straight waveguide structures are presented, while Section 5.3 discusses the results obtained for the unbalanced Mach-Zehnder interferometer structure with multiple measurands. The chapter concludes with Section 5.4, where the results obtained are summarized and extended through simulation, and suggestions for future improvements of the design are given.

5.1 Measurement Setup

Optical device testing was performed at the National Research Council optical testing laboratory. The measurement setup is shown in Figure 5.1. An Agilent 81682A tunable laser with a 1470 – 1580 nm range was used as the light source during the measurements. The signal from the laser source is transmitted through an in-line polarizer set to TM polarization, and butt-coupled to the test device using a Namiki polarization-maintaining (PM) tapered single-mode fiber. The sample under test is positioned on a stage, and the output light from the sample is collected using a 20× objective lens. The output power is measured using an Agilent 815224A

high sensitivity InGaAs detector, or reflected to a Sensors Unlimited SU320M-1.7RT InGaAs near infra-red mini-camera for visual inspection.

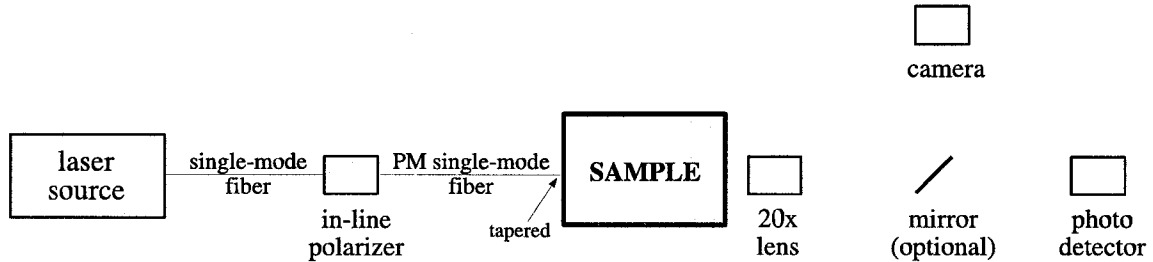


Figure 5.1: National Research Council optical measurement setup.

The positions of the tapered input fiber, the sample stage and the lens can be controlled using individual positioners in order to align the components such that light is properly coupled into the waveguide and captured by the photodetector. Note that although the setup is mounted on a vibration-isolated optical bench, the sample itself is not fixed on the stage. Therefore, any vibration or movement of the setup can potentially change the alignment between the components requiring a realignment of the system. Optimal alignment was obtained by first getting the waveguide device to guide light, which was visually confirmed by viewing the output power using the infra-red camera. Then the positioners of the input fiber and the lens were adjusted until maximum power was detected by the photodetector.

5.2 Waveguide Measurements

Straight waveguide structures were measured first to ensure that the fabricated devices guide light and to measure the additional power loss incurred due to the perforations. Typical straight waveguide losses were measured to be in the range 18 – 26 dB for TM polarization. This loss is a combination of five main factors:

1. Losses due to the measurement setup – a typical reference measurement of the system shows ~ 4 dB loss due to losses in fiber connectors, polarizing optics, output lens optics and other components.

2. Fresnel reflection losses at the facets of the sample – in Section 4.2 power loss due to the Fresnel reflections was calculated to be ~ 1.6 dB per facet, resulting in total loss of ~ 3.2 dB.
3. Mode mismatch between the input fiber and the waveguide – as previously discussed in Section 4.2, the large mismatch in the mode size between an SOI waveguide and a single-mode optical fiber causes reduced coupling efficiency.
4. Propagation losses – losses that occur due to fabrication defects such as waveguide surface and sidewall roughness, leakage of optical power to the silicon substrate, and other factors. Based on previous projects that have used the microfabrication facilities at Carleton University, the propagation loss can be estimated to be 2 dB/cm, or ~ 5 dB loss for the entire sample.
5. Quality of the waveguide facets – although effort was made to create smooth end-face cleaves, successful cleaves were not achieved every time, resulting in rugged facets that cause significant light scattering.

The additional power loss due to the perforations was measured by comparing the optical power transmitted by a perforated waveguide to the power transmitted by a standard waveguide, as shown in Figure 5.2. Both waveguides have the same dimensions, and are located on the same sample. The reference standard waveguide compensates for any losses in the experimental setup, reflections of sample facets, and other factors. The spectra shown in Figure 5.2 indicate that the loss in the perforated waveguide is ~ 7.5 dB higher than the loss in the standard waveguide. In Subsection 3.2.3 the perforated waveguide loss was simulated by OptiFDTD and FIMMPROP to be 2.6 dB and 4 dB, respectively. The 3.5 – 4.9 dB higher loss in the measurements may be partially attributed to sidewall roughness of the perforations, a parameter that was not accounted for in the simulations. However, because of the small number of available samples and the presence of a number of mechanisms that may affect the losses in the fabricated waveguides (e.g. varying cleave quality, fabrication defects, etc.), the measurements shown in Figure 5.2 cannot be used as a

conclusive indication of the extra losses incurred due to the perforations. A greater number of samples need to be fabricated to obtain statistically significant results.

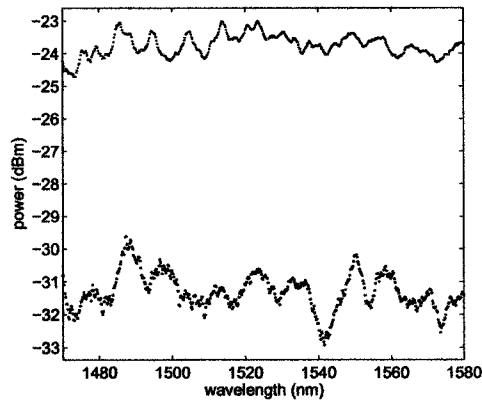


Figure 5.2: Measured power spectra of a standard waveguide (red trace) and a perforated waveguide (blue trace).

5.3 Unbalanced Mach-Zehnder Interferometer Measurements

The sensitivity of the perforated region to the refractive index of the upper cladding was studied by examining the output intensity of the unbalanced Mach-Zehnder interferometer as a function of wavelength. In all measurements the reference arm of the interferometer was covered with a protective layer of S1811 photoresist. Note, however, that it is expected that a negligible amount of S1811 gets into the perforations in the reference arm during the process of spinning of the photoresist due to the behavior of liquids as described in Section 2.3. Therefore, the reference arm has *air* in the perforations, and S1811 as cladding material elsewhere. Also, in all measurements the shorter arm of the unbalanced MZI was used as the reference arm, while the longer arm served as the sensing arm. The materials used as the upper cladding for the exposed sensing arm are air and de-ionized water.

During the first few measurement attempts, the following measurement process was used:

1. Starting from a dry SOI sample with air as upper cladding, align the input and output of the unbalanced MZI with the measurement system components.
2. Measure the power spectrum of the unbalanced MZI for a range of wavelengths.
3. Place a drop of de-ionized water on top of the sensing arm of the interferometer.
4. Realign the input and output of the unbalanced MZI with the measurement system components.
5. Measure the power spectrum of the unbalanced MZI for a range of wavelengths.

Note that realignment of the sample after introducing water was required because the sample was not secured on the sample stage. In all cases, optimal alignment was achieved by visually aligning the input fiber and the output lens, and adjusting the system components such that maximum power is detected by the photodetector.

Although a shift was observed in the spectrum when a drop of water was placed on the sample, a question arose as to whether the water was able to fully fill the perforations in the sensing arm. As described in Section 2.3, trapped air inside the perforations slows down the flow of water, and complete filling of the perforations occurs only after the air slowly dissolves in the liquid. Note that the length of the perforated region is only $100\ \mu\text{m}$, while the width of the sensing windows (see Figure 4.6) is 1 mm, thus there is a 0.9 mm interaction length between the cladding material and the evanescent field of a standard (i.e. non-perforated) waveguide mode. Therefore, although the predicted sensitivity of the non-perforated region is lower than that of the perforated region, because of the longer interaction length between the standard waveguide and the water cladding its effect may become significant, also causing a shift in the output spectrum.

To answer the above question, a method was needed to ensure that water fully fills the perforations. Following the advice of Professor J. Gaydos from the Department

of Mechanical and Aerospace Engineering, the SOI sample was subjected to a cold-boiling process in de-ionized water. The boiling point is defined as the temperature at which the saturated vapor pressure of a liquid is equal to the surrounding atmospheric pressure [57]. For water, the vapor pressure reaches the standard sea level atmospheric pressure of 760 mmHg at 100° C. Since the vapor pressure increases with temperature, it follows that the boiling point varies with pressure. When the surrounding pressure is reduced to 24 mmHg, the boiling point of water occurs at room temperature (25° C), a process referred to as 'cold-boiling'. The boiling process allows the trapped air to rise up to the surface, thus letting the water to fully fill the perforations.

The sample measurement process was thus refined as following:

1. Starting from a dry SOI sample with air as upper cladding, align the input and output of the unbalanced MZI with the measurement system components.
2. Measure the power spectrum of the unbalanced MZI for a range of wavelengths.
3. Submerge sample in de-ionized water at room temperature, and place the container in a vacuum chamber. Reduce the chamber pressure to ~ 24 mmHg, until the water begins to cold-boil. Continue boiling for about 5 minutes.
4. Leave sample in de-ionized water until measurement time (typically overnight).
5. Remove sample from water and align the input and output of the unbalanced MZI with the measurement system components. Add a droplet of water on the sample every few minutes to keep water cladding from evaporating.
6. Measure the power spectrum of the unbalanced MZI for a range of wavelengths.

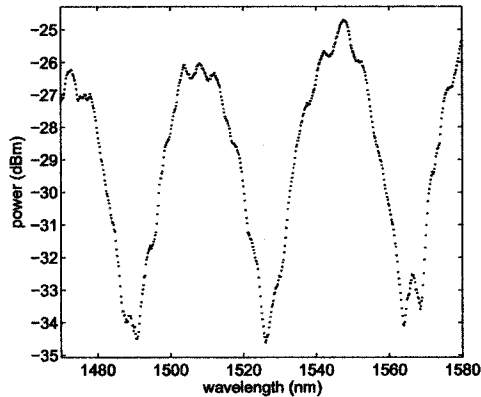
Figure 5.3(a) shows the power spectrum obtained with a perforated unbalanced MZI device with air as the upper cladding in the sensing arm. The experimental measurement shows modulation depth of ~ 8.5 dB. An ideal low-pass Fourier filter (cut-off frequency 32.82 MHz) implemented in MATLAB was used to remove the high-frequency noise from the waveform in Figure 5.3(a), allowing one to see the modulation due to the interference between the two arms of the interferometer more clearly, as shown in Figure 5.3(b).

Equation (2.35) was used to estimate the path length difference between the two arms of the interferometer based on the spectrum in Figure 5.3(b), resulting in $\Delta L \approx 17.39 \mu\text{m}$. To determine a more precise figure for the path difference, a fit between a mathematical expression for the transmission power of an unbalanced MZI (equation (2.30)) and the filtered experimental modulation waveform shown in Figure 5.3(b) was performed. A least-squares method was used to find the path length parameter ΔL in the mathematical model that best fits the wavelength locations of the minima and the maxima points of the filtered spectrum. The best fit was found with path length difference $\Delta L = 17.40 \mu\text{m}$, shown in Figure 5.3(c).

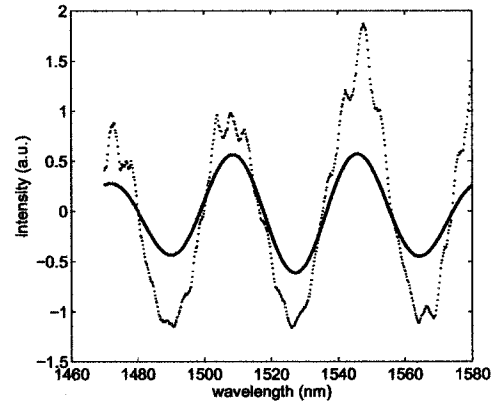
Note that although the path length difference between the two arms of the interferometer should be closer to $13.87 \mu\text{m}$ (calculated from the mask layout in Section 3.3) rather than $17.40 \mu\text{m}$, it is not unusual to find effective path length differences even between two nominally symmetric arms of an interferometer device [23]. Effective path difference may be introduced due to defects during fabrication, such as imperfect power splitters, variations in the waveguide profile, uneven sidewall roughness and local variations in the thickness of the guiding silicon layer. Even a small imbalance in the optical loss of the two arms could increase or decrease the imbalance of the MZI. In the current design, the slightly different distribution of the pseudo-random perforations in the two arms of the interferometer can also contribute to an additional imbalance of the MZI.

Figure 5.4(a) shows again the power spectrum obtained with a perforated unbalanced MZI device with air as upper cladding (case 1), along with two additional curves – the blue curve correspond to the spectrum measured when a drop of water is added on top of the previously dry sensing arm of the device (case 2), and the green curve corresponds to the spectrum measured when the sample was cold-boiled and soaked in de-ionized water (case 3). Note that in this case it is difficult to make a direct comparison between the absolute power of the modulation spectra for different measurements. The absolute power is highly dependent on the alignment between the system components, and thus it is the variation of the spectrum with respect to the wavelength axis that serves as a comparison between the measurements.

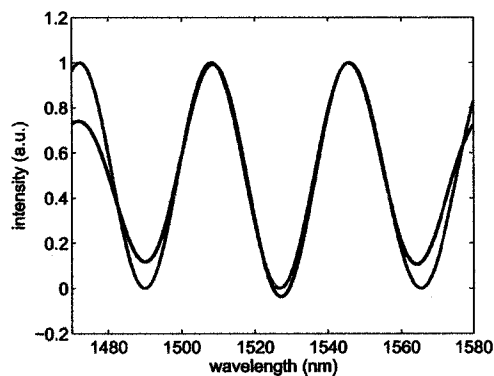
The presence of noise in the signals shown in Figure 5.4(a) makes the measurement



(a) Measured power spectrum.



(b) Measured power spectrum (red trace) and measured power spectrum with high-frequency noise filtered out (black line).

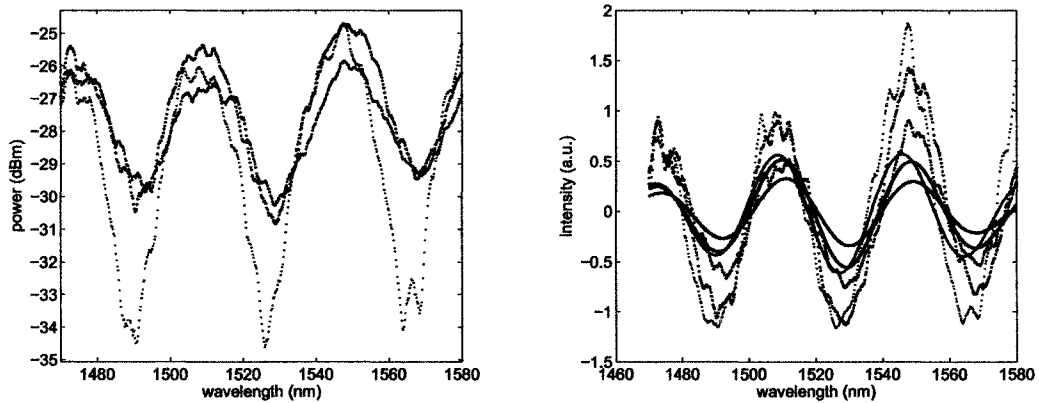


(c) Filtered power spectrum (black line) and a best fit based on the mathematical model of the Mach-Zehnder interferometer (red line).

Figure 5.3: Measured power spectrum of the perforated Mach-Zehnder interferometer with air as upper cladding.

of a shift between the waveforms difficult. Filtering of the high-frequency noise in the signals using a low-pass filter implemented in MATLAB (with the cut-off frequency as determined from the reference signal shown in Figure 5.3) produces a much clearer

picture of the three waveforms as shown in Figure 5.4(b). At a wavelength of $1.55 \mu\text{m}$, spectrum shift of 2.6 nm is measured between the first two cases, and an additional shift of 0.6 nm is measured between the second and third cases.



(a) Measured power spectra: case 1 (red trace), case 2 (blue trace) and case 3 (green trace).

(b) Measured power spectra for cases 1, 2 and 3, and the corresponding waveforms with high-frequency noise removed.

Figure 5.4: Measured power spectra of the perforated Mach-Zehnder interferometer with air and water as upper cladding.

Note that the additional spectrum shift between cases 2 and 3 indicates that in the case 2 scenario (a drop of water placed on top of a previously dry perforated sensing arm), while the water filled in the sensing window, it did not fully fill the perforations. The liquid dynamics theory presented in Section 2.3 qualitatively explains that penetration of water into a perforation with one exit is governed first by a fast process, during which the water partially fills the perforations due to capillary-driven forces, followed by a much slower process, where the trapped air in the perforations is slowly dissolved in the water. Although quantitatively, the model predicts that the perforations will fully fill within seconds, the model has been shown to grossly underestimate the time required for the liquid to fill porous materials, and it cannot be used for reliable quantitative predictions of liquid behavior. From the obtained measurements it can be concluded that in case 2 the water only partially fills the per-

forations, leaving trapped air at the bottom of the perforations, precisely in the area where the evanescent field is present. As a result, in the perforated waveguide region the evanescent field propagates through air, not water. Therefore the shift observed in Figure 5.4(b) between cases 1 and 2 (red and blue curves) can only be attributed to the evanescent wave sensing of the water in the *standard* (i.e. the *non-perforated*) waveguide region.

In case 3, however, the cold-boiling and the prolonged soak of the sample allows the water to fully fill the perforations. The shift observed between cases 2 and 3 (blue and green curves in Figure 5.4(b)) therefore indicates the change in the effective index of the propagating mode as it travels down the *perforated* region. The simulations described in Section 3.3 modeled this shift as being 0.48 nm based on OptiFDTD results, and 0.97 nm based on FIMMPROP results, compared to the 0.6 nm shift measured during the actual experiments.

The observed shifts between the three cases can also be used to estimate the relative sensitivity of the standard and the perforated regions of the interferometer. Assuming that the water that partially fills the perforations in case 2 has a negligible effect on the optical signal as it travels through the perforated region, the shift of 2.6 nm can be attributed to the evanescent field sensing of the standard waveguide region, which is 0.9 mm long. The additional 0.6 nm shift can be attributed to the evanescent field sensing in the 100 μm long perforated waveguide region. These numbers indicate that the perforated waveguide region is about twice as sensitive as the standard waveguide region. Although the measurements and the simulations agree in that the perforated waveguide region is more sensitive to the refractive index of the surrounding material, the relative increase in sensitivity predicted by simulations is higher (~ 5 times based on OptiFDTD and ~ 8 times based on FIMMPROP).

In order to verify that the observed shifts in the measured spectra are indeed the result of the change in the measurand and not due to thermal effects, a quick analysis of the temperature effects on the properties of silicon is presented next. The change in the optical path length in silicon is dominated by the temperature dependence of its refractive index, with a smaller contribution from thermal expansion. For small temperature variations, a change in the refractive index is linearly proportional to

the change in temperature as given by equation (5.1) [58]:

$$\Delta n_{Si} = 1.8 \times 10^{-4} \Delta T \quad (5.1)$$

where ΔT is given in degrees Celsius, and the expression is valid for operation near room temperature. For a variation of up to 2° C in the room temperature that may be present between different measurements, $\Delta n_{Si} = 3.6 \times 10^{-4}$ may be expected. This change in the refractive index of silicon will cause a change in the effective index of the propagating mode n_{eff} , where the upper bound on this change is given by $\Delta n_{eff} = \Delta n_{Si} = 3.6 \times 10^{-4}$. This change in the effective index will induce a change in optical path length between the two arms of the interferometer, thus resulting in a maximum 0.16 nm shift in the Mach-Zehnder interferometer output spectrum.

The thermal expansion coefficient of silicon is given by $\alpha = 2.6 \times 10^{-6} \text{ }^\circ\text{C}^{-1}$ near room temperature operation [58], thus for a maximum change of 2° C in the measurement environment, the change in the physical path length difference between the two arms is below 0.1 nm, resulting in maximum spectrum shift of 0.01 nm. Therefore, since the maximum shifts in the interferometer output spectrum that may be induced by the thermal variations in the measurement environment are significantly lower than the shifts in Figure 5.4(b), it can be concluded that the measured shifts are dominated by the change in the effective index induced by the change in the measurand.

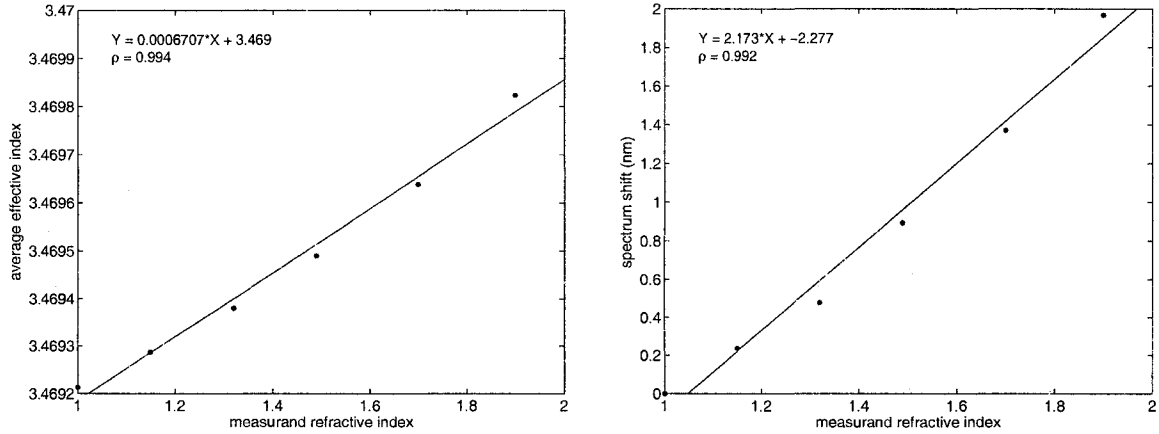
5.4 Discussion of Results

The experimental measurements, as presented in Sections 5.2 and 5.3, are in reasonable agreement with the simulation work described in Chapter 3. Qualitatively, both the experimental evidence and the simulations agree that the perforated waveguide region proposed in this project is more sensitive to variations in the refractive index of the upper cladding material than a standard waveguide with the same dimensions. Quantitatively, however, while simulations predict that the relative sensitivity is 5 – 8 times greater for the perforated waveguide, experiments show only an increase

by a factor of 2. The extra loss in a perforated waveguide relative to a standard waveguide was measured to be ~ 7.5 dB, compared to 2.6 – 4 dB predicted by simulations. While the larger measured loss may be partially attributed to the scattering of light due to roughness of the perforation walls, this measurement is not conclusive as the results could not be confirmed with a larger number of waveguides due to a limited number of available samples. In terms of the shift in the output spectrum of the unbalanced MZI when the cladding material in the perforated region of the sensing arm is changed from air to water, the experimental shift of 0.6 nm agreed well with the simulated 0.48 – 0.97 nm shift.

Although the two-dimensional beam propagation simulation results suggested that a higher-order mode is excited at the output of the unbalanced Mach-Zehnder interferometer (see Figure 3.8), the presence of a significant modulation depth in the measured spectra of the device suggest that the optical signal propagates as a fundamental mode throughout the structure. The inaccuracy in the OptiBPM beam propagation simulation is likely to be a result of the limitations of the effective index method (EIM) approximation. The EIM assumes that the waveguides are weakly guiding [59], which is not the case for SOI-based rib waveguides, leading to inaccuracies in the simulated waveguide behavior [60].

Due to the available time frame, the experimental measurements studied the response of the fabricated sensor structure only for air and de-ionized water. However, since the measurement results agreed well with the simulations in terms of the shift in the output spectrum of the device, simulations can be used to further predict the behavior of the device for measurands with other refractive indices. OptiFDTD simulation results for measurand refractive indices in the range 1 – 1.9 and their effect on the average effective index of the mode are shown in Figure 5.5(a). Figure 5.5(b) shows the corresponding simulated shift of the MZI output spectrum as a function of the refractive index of the measurand. In the context of Figure 5.5(b) the sensitivity of the sensor can be defined as the change in the spectrum shift due to a change in the refractive index of the measurand [61], and evaluated based on the linear fit to be ~ 2.2 nm/RIU. A reasonable estimate of the minimum detectable refractive index change is $\sim 5 \times 10^{-2}$.



(a) Change in the average effective index of a mode in a perforated waveguide structure as a function of the refractive index of the measurand (based on OptiFDTD simulations). Solid line shows a least-squares linear fit to the data with correlation parameter $\rho = 0.994$.

(b) Expected spectrum shift of the unbalanced Mach-Zehnder interferometer sensor as a function of the refractive index of the measurand (based on OptiFDTD simulations). Solid line shows a least-squares linear fit to the data with correlation parameter $\rho = 0.992$.

Figure 5.5: Simulated sensor device behavior for measurands with different refractive indices.

During the early stages of this project, the intention was to use the unbalanced MZI structure in preliminary tests to verify that the device indeed works as a refractive index sensor, and then to switch to the balanced MZI structure for the actual measurements, where the intensity of the output at a given wavelength would be a function of the refractive index of the measurand. However, it was realized that because of a very short interaction length, the variation in the output signal is very small. In this case the balanced MZI would produce a minimal change in the intensity of the output signal for a given wavelength, since the device is biased around the $\Delta\phi = 0$ point, where the sensitivity to changes in the phase difference between the two arms (i.e. the slope in Figure 2.6(b)) is close to zero. Therefore, due to the low sensitivity of the balanced MZI structure, coupled with the noise present in the measured signal, detecting small differences in the output intensity would be very difficult, if not impossible. The use of the unbalanced MZI, however, gives the

advantage that even a small shift in the spectrum can be measured.

Although the use of longer interaction length will result in a larger shift and thus higher sensitivity, the high diffraction losses inherent to the perforated structure limit the maximum interaction length that can be used in practice. This defines the major problem in the proposed device – the chosen fabrication process limited the minimum diameter of the perforations to $0.3 \mu\text{m}$, value that is comparable to the wavelength of light in the waveguide ($\sim 0.45 \mu\text{m}$), thus resulting in high losses. In hindsight, alternative fabrication techniques should have been considered such that the perforations are much smaller than the wavelength of operation. One way of creating smaller perforations in the silicon waveguides is to use porous silicon. Porous silicon is composed of a silicon skeleton permeated by a network of pores, typically fabricated by electro-chemical anodization of silicon in a hydrofluoric acid (HF) based electrolyte. The factors that determine the physical characteristics of the porosity are well-characterized, allowing great control over the porosity of the fabricated material [62].

Porous material can be treated as a macroscopically inhomogeneous medium [63], i.e. a medium in which quantities such as the refractive index vary in space, whose refractive index can be estimated by the Bruggemann's effective medium approximation, given by [64]:

$$p \frac{n_{\text{pore}}^2 - n_{\text{material}}^2}{n_{\text{pore}}^2 + 2n_{\text{material}}^2} + (1 - p) \frac{n_{\text{branch}}^2 - n_{\text{material}}^2}{n_{\text{branch}}^2 + 2n_{\text{material}}^2} = 0 \quad (5.2)$$

where n_{material} , n_{material} and n_{pore} are the refractive indices of the porous material, the branches of the material, and the pores of the material, respectively, and p is the porosity of the material (defined as the ratio between the volume of the pores and the volume of the entire material). Replacing the air in the pores of the silicon with an alternative material will cause a change in the refractive index of the porous silicon layer, which in turn causes a change in the optical characteristics of the guided mode. This is the exact mechanism investigated in this project, only in this case the perforations are of much larger scale, and fabricated by means of electron-beam lithography. In both cases, the motivation behind using a porous / perforated waveguide arises from the fact that the measurand interacts with a more substantial portion of the

guided mode, and not just the evanescent tail as is the case with standard waveguide evanescent field sensors, thus potentially having greater sensitivity. For example, porous silicon with $p = 0.65$ and air in the pores, according to equation (5.2), has an estimated refractive index of 1.70, while the same structure with water in the pores has a refractive index of about 1.97. This large change in the refractive index means that high sensitivity can be achieved with relatively short interaction lengths.

Note that when the perforations are made much smaller, as is the case with porous silicon (e.g. meso-porous silicon pore diameter can range between 5 and 70 nm), they do not greatly contribute to light scattering because of their small size compared to the operating wavelength. Therefore, a sensing region with very small perforations can be used over long interaction lengths, unlike the current design where light scattering due to the perforations restricts the maximum length of the interaction region. A known problem with porous silicon material is its rapid degradation, however, oxidation techniques have been recently demonstrated that stabilize the porous silicon material against corrosion and degradation in biological solutions [62]. Note also that the small diameter of the pores further aggravates the problem of liquid penetration into the pores, as discussed in this project, and a number of research groups are investigating this issue in the context of biomedical device applications [62] [65].

A number of other alternatives can be explored to reduce the diffraction losses of the perforated waveguide structure. One approach would be to use lower contrast waveguide materials, where on one hand the mode field is less confined and thus has larger evanescent field, and on the other hand the scattering losses can be significantly lower than in high-contrast structures. The dimensions of the perforations and their placement can be also optimized by exploring the resonance behavior of the perforations, similar to the analysis performed in the context of periodically segmented waveguides in [8]. In terms of simulating the behavior of the perforated region, while it was shown in this thesis that three-dimensional optical simulations can be successfully used, it would also be worthwhile to explore other, potentially more stable and time-efficient simulation methods. One example could be representing the perforations as five-layer slab waveguides, which reduces the three-dimensional problem to two dimensions.

While the sensitivity of the fabricated sensor devices is low compared to other implementations, it should be noted that these devices represent a proof-of-concept project, which attempts to assess the feasibility of using a perforated waveguide structure as means of increasing the sensitivity of an interferometer-based refractive index sensor device. In a proof-of-concept project, it is important to identify a process that can be used to analyze the proposed structure, which has been done and presented in detail in this report. Note that in the current implementation, the waveguide dimensions and the geometrical parameters of the interferometer structure were largely determined by financial considerations (availability of certain SOI material and mask), rather than by optimizations through extensive analysis. Yet, the fabricated structure clearly demonstrates that a perforated waveguide region is more sensitive to variations in the refractive index of the cladding than a standard waveguide. Therefore with a more optimized design, where some suggestions for optimization are mentioned above, it can be expected that the sensitivity of a sensor device based on the perforated waveguide structure can be significantly improved.

Chapter 6

Conclusions and Recommendations

In this thesis an evanescent field refractive index sensor based on a perforated Mach-Zehnder interferometer structure implemented in a silicon-on-insulator (SOI) rib waveguide is investigated. When an optical mode propagates through an SOI waveguide, it is mostly confined to the silicon core guiding layer, but some portion of the mode, known as the evanescent field, extends into the cladding regions of the waveguide, where it decays in an exponential fashion. Because the evanescent field propagates outside the waveguide core, it can interact with the surrounding medium. In a typical waveguide the fraction of the mode that propagates outside the core as an evanescent wave is very small, thus evanescent field sensors require long interaction length between the mode and the material to be measured (the measurand) to achieve a significant cumulative effect.

The goal of this project is to find a mechanism that would increase the portion of the guided mode that travels in the cladding, given that the dimensions of the waveguide should remain fairly large to facilitate efficient light coupling between the waveguide-based sensor device and the input / output optical fibers. The mechanism that is investigated in this project involves perforating the waveguide core such that a larger portion of the mode field is forced out of the silicon and into the cladding.

When a measurand is introduced as the waveguide cladding material, a variation in the effective index of the guided mode is induced. To measure this change in the effective index, this project utilizes an unbalanced Mach-Zehnder interferometer

structure, where both arms of the interferometer contain a perforated waveguide region. The measurand is introduced as the cladding material of the sensing arm of the interferometer, while the second arm is protected from the measurand and thus is kept in a constant reference state. The interference between the signals in the two arms at the output waveguide of the interferometer is used to infer the change in the refractive index of the measurand.

Analysis of the proposed device was performed using both analytical models and numerical simulations. The effects of the waveguide perforations were investigated through three-dimensional finite-difference time-domain and eigenmode expansion method simulations. This included studying the effect of the perforations on the average effective index of the guided mode, and the optical loss introduced as a result of the perforations. To simulate the behavior of the complete Mach-Zehnder sensor structure, two-dimensional beam propagation simulations and analytical models were used.

The devices were fabricated in a three-stage process. First, the perforated region was fabricated using electron-beam lithography and ECR plasma etching. Next, the interferometer structure was fabricated using UV lithography and ECR plasma etch. The sensing windows structure, which allows the measurand to be introduced only to the required areas on the sample, was patterned last using a UV lithography process.

The experimental measurements have shown reasonable agreement with simulations. The scattering loss due to the waveguide perforations was measured to be 7.5 dB, about twice the value predicted by simulations. This discrepancy may be partially attributed to the sidewall roughness of the perforations, a parameter that was not accounted for in the simulations. However, because of the small number of available samples, this measurement could not be confirmed with statistically significant number of waveguides. Both the simulations and the experimental results agreed that the perforated waveguide is more sensitive to variation in the refractive index changes of the cladding than a standard waveguide with the same dimensions, satisfying the main goal of the project. However, while the simulation predicted the perforated structure to be 5 – 8 times more sensitive, experimental measurements have shown only an increase by a factor of two. When the measurand was changed from air to

water, a 0.6 nm shift of the Mach-Zehnder interferometer output spectrum with respect to the wavelength axis was measured, agreeing well with the shift predicted by simulations.

Extrapolation of the sensor behavior through three-dimensional finite-difference time-domain simulation predicted a 2.2 nm shift per unit refractive index change of the measurand. While high sensitivity was not obtained with the sensor introduced here, this project adequately demonstrates that the perforated waveguide structure increases the sensitivity of the guided mode to variations in the refractive index of the surrounding medium, and thus is a suitable structure for evanescent field sensing.

The major obstacle in utilizing the perforated structure over longer interaction lengths is the large scattering loss due to the perforations. A number of improvements are suggested over the current design. First, reducing the size of the perforations such that they are much smaller than the wavelength of operation will significantly reduce the scattering losses. This would require a change in the fabrication process used to create the perforations; one possibility is to use porous silicon. Alternatively, the dimensions and placement of the perforations can be optimized by exploring their resonance behavior, or the loss can be reduced by using waveguide materials of lower refractive index contrast. Moreover, while the perforated structure can be successfully modeled using three-dimensional simulation tools as was described in this thesis, other simulation techniques can be explored, where the problem is modeled in two dimensions, potentially leading to more stable and less resource intensive simulations. A more optimized design of the perforated Mach-Zehnder interferometer sensor based on the recommendations described above and a longer perforated interaction region are expected to result in a significant sensitivity increase over the current design.

Appendix A

List of Acronyms

APSS	Apollo Photonic Solutions Suite
BPM	Beam Propagation Method
DC	Direct Current
DFT	Discrete Fourier Transform
ECR	Electron Cyclotron Resonance
EIM	Effective Index Method
FDTD	Finite Difference Time Domain
FEM	Finite Element Method
FMM	Film Mode Matching
HF	Hydrofluoric Acid
HMDS	Hexamethyldisilazane
IOI	Input Overlap Integral
IPA	Isopropyl Alcohol
MZI	Mach-Zehnder Interferometer
NPGS	Nanometer Pattern Generation Software

PM	Polarization Maintaining
RF	Radio Frequency
RIU	Refractive Index Unit
rpm	Revolutions Per Minute
sccm	Standard Cubic Centimeters per Minute
SEM	Scanning Electron Microscope
SOI	Silicon On Insulator
TE	Transverse Electric
TM	Transverse Magnetic
UV	Ultraviolet

Appendix B

Device Process Flow

The following is the complete process used in the fabrication of the perforated Mach-Zehnder interferometer sensor device studied in this project:

Stage 1 – Fabrication of the Perforated Region

1. Pre-bake (oven at 180° C for 2 hours or 220° C for 15 minutes)
2. Spin HMDS (5000 rpm, no wobble) + soft-bake (hotplate 105° C for 1 minute)
Spin Zep (5000 rpm, no wobble) + soft-bake (hotplate 180° C for 5 minutes)
3. SEM write (39 kV acceleration voltage, 900 magnification, 200 $\mu\text{C}/\text{cm}^2$ area dose, 3 pA measured beam current)
4. Develop Zep (o-xylene for 2 minutes + IPA for 1 minute)
5. Descum (0.3 T, 100 W for 10 seconds)
6. Stick sample on a 100 mm backing wafer using carbon tape
7. ECR etch ($\text{SF}_6:\text{O}_2 = 3.65 : 2.21$, 6 mTorr, -30°C , 4.5 minutes)
8. Remove sample from backing wafer (heat on hotplate until lifts or soak in acetone overnight)
9. Remove photoresist using Caro's acid

Stage 2 – Fabrication of the Interferometer Device

10. Pre-bake (oven at 250° C for 30 minutes)
11. Spin HMDS (4000 rpm, wobble) + soft-bake (hotplate 105° C for 1 minute)
Spin S1811 (4000 rpm, wobble) + soft-bake (hotplate 105° C for 1 minutes)
12. Expose waveguides (15 seconds, 16 mW/cm² lamp intensity)
13. Develop S1811 (MF321 for 1 minute + water for 1 minute)
14. Hard-bake (hotplate 115° C for 3 minutes)
15. Descum (0.3 T, 100 W for 10 seconds)
16. Stick sample on a 100 mm backing wafer using carbon tape
17. ECR etch (SF₆:O₂ = 3.65 : 2.21, 6 mTorr, -30° C, 2.4 minutes)
18. Remove sample from backing wafer (heat on hotplate until lifts or soak in acetone overnight)
19. Remove photoresist using Caro's acid
20. Thin sample to 250 μm thickness using grinding wheel (220 grit paper for 10 minutes × 2, 0.4 DC mA, 1.85 kg weight)
21. Cleave sample at input and output edges
22. Remove adhesive remnants using Caro's acid

Stage 3 – Fabrication of the Sensing Windows

23. Pre-bake (oven at 250° C for 30 minutes)
24. Spin S1811 (4000 rpm, wobble) + soft-bake (hotplate 105° C for 1 minutes)
25. Expose sensing windows (20 seconds, 16 mW/cm² lamp intensity)
26. Develop S1811 (MF321 for 1 minute + water for 1 minute)
27. Hard-bake (hotplate 115° C for 4 minutes)
28. Descum (0.3 T, 100 W for 3 minutes)

Bibliography

- [1] E. Udd. *Fiber Optic Sensors – An Introduction for Engineers and Scientists*. Wiley-Interscience, 1991.
- [2] G. T. Reed and A. P. Knights. *Silicon Photonics: An Introduction*. John Wiley & Sons Ltd, 2004.
- [3] G. Celler and S. Christoloveanu. Frontiers of silicon-on-insulator. *Applied Physics*, 93(9):4955–4978, 2003.
- [4] A. S. Sedra and K. C. Smith. *Microelectronic Circuits*. Oxford University Press, fourth edition, 1998.
- [5] P. V. Lambeck. Integrated optical sensors for the chemical domain. *Measurement Science and Technology*, 17(8):R93–R116, August 2006.
- [6] F. Prieto, B. Sepulveda, A. Calle, A. Llobera, C. Dominguez, A. Abad, A. Montoya and L. M. Lechuga. An integrated optical interferometric nanodevice based on silicon technology for biosensor applications. *Nanotechnology*, 14(8):907–912, August 2003.
- [7] F. Prieto, B. Sepulveda, A. Calle, A. Llobera, C. Dominguez and L. M. Lechuga. Integrated Mach-Zehnder interferometer based on ARROW structures for biosensor applications. *Sensors and Actuators B*, 92(1–2):151–158, July 2003.
- [8] N. Kinrot. Analysis of bulk material sensing using a periodically segmented waveguide Mach-Zehnder interferometer for biosensing. *Journal of Lightwave Technology*, 22(10):2296–2301, 2004.

- [9] D. Esinenco, S. D. Psoma, M. Kusko, A. Schneider and R. Muller. SU-8 micro-biosensor based on Mach-Zehnder interferometer. *Reviews on Advanced Materials Science*, 10(4):295–299, October 2005.
- [10] A. Brandenburg. Differential refractometry by an integrated-optical Young interferometer. *Sensors and Actuators B*, 39(1–3):266–271, March 1997.
- [11] D. Hofstetter, H. P. Zappe and R. Dandliker. A monolithically integrated double Michelson interferometer for optical displacement measurement with direction determination. *IEEE Photonics Technology Letters*, 8(10):1370–1372, 1996.
- [12] C. Stamm and W. Lukosz. Integrated optical difference interferometer as refractometer and chemical sensor. *Sensors and Actuators B*, 11(1–3):177–181, March 1993.
- [13] D. A. Cohen, C. S. Wang, J. A. Nolde, D. D. Lofgreen and L. A. Coldren. Monolithic evanescent field spore detector. In *Proceedings of the Integrated Photonics Research*, number IThB3, June 2004.
- [14] E. Krioukov, D. J. W. Klunder, A. Driessen, J. Greve and C. Otto. Sensor based on an integrated optical microcavity. *Optics Letters*, 27(7):512–514, 2002.
- [15] R. W. Boyd and J. E. Heebner. Sensitive disk resonator photonic biosensor. *Applied Optics*, 40(31):5742–5747, 2001.
- [16] R. E. Kunz, J. Edinger, P. Sixt and M. T. Gale. Replicated chirped waveguide gratings for optical sensing applications. *Sensors and Actuators A*, 47(1–3):482–486, March–April 1995.
- [17] J. Homola, S. Yee and G. Gauglitz. Surface plasmon resonance sensors: review. *Sensors and Actuators B*, 54(1–2):3–15, January 1999.
- [18] P. Bienstman, F. Van Laere, D. Taillaert, P. Dumon, W. Bogaerts, K. De Vos, D. Van Thourhout and R. Baets. High index-contrast silicon-on-insulator nanophotonics. In *Proceedings of the International Conference on Transparent Optical Networks*, number Tu.D2.1, pages 124–127, 2006.

- [19] D.-X. Xu, A. Densmore, J. Lapointe, P. Waldron, P. Cheben, A. Delage, B. Lamontagne, S. Janz, J. H. Schmid and E. Post. High index contrast photonic waveguide components for biological sensing (submitted abstract). In *The Electrochemical Society Transactions*, 2006.
- [20] G. P. Agrawal. *Lightwave Technology*. Wiley-Interscience, 2004.
- [21] U. S. Inan and A. S. Inan. *Electromagnetic Waves*. Prentice Hall, 1999.
- [22] H. Kogelnik and V. Ramaswamy. Scaling rules for thin-film optical waveguides. *Applied Optics*, 13(8):1857–1862, 1974.
- [23] P. Waldron. *Optimization of Plasma Dispersion Modulators in Silicon-on-Insulator*. PhD thesis, McMaster University, 2005.
- [24] R. A. Soref, J. Schmidtchen and K. Petermann. Large single-mode rib waveguides in GeSi-Si and Si-on-SiO₂. *IEEE Journal of Quantum Electronics*, 27(8):1971–1974, 1991.
- [25] S. P. Pogossian, L. Vescan and A. Vonsovici. The single-mode condition for semiconductor rib waveguides with large cross section. *Journal of Lightwave Technology*, 16(10):1851–1853, 1998.
- [26] A. G. Rickman, G. Reed and F. Namavar. Silicon-on-insulator optical rib waveguide loss and mode characteristics. *Journal of Lightwave Technology*, 12(10):1771–1776, 1994.
- [27] H. Porte, V. Gorel, S. Kiryenko, J. P. Geodgebuer, W. Daniau and P. Blind. Imbalanced Mach-Zehnder interferometer integrated in micromachined silicon substrate for pressure sensor. *Journal of Lightwave Technology*, 17(2):229–233, 1999.
- [28] E. F. Schipper, A. M. Brugman, C. Dominguez, L. M. Lechuga, R. P. H. Kooyman and J. Greve. The realization of an integrated Mach-Zehnder waveguide immunosensor in silicon technology. *Sensors and Actuators B*, 40(2–3):147–153, May 1997.

- [29] J. J. Lillie, M. A. Thomas, N. M. Jokerst, S. E. Ralph, K. A. Dennis and C. L. Henderson. Multimode interferometric sensors on silicon optimized for fully integrated complementary-metal-oxide-semiconductor chemical-biological sensor systems. *Journal of the Optical Society of America B*, 23(4):642–651, April 2006.
- [30] S. M. Iveson, K. F. Rutherford and S. R. Biggs. Liquid penetration rate into submerged porous particles: theory, experimental validation and implications for iron ore granulation and sintering. *Mineral Processing and Extractive Metallurgy*, 110(3):133–143, December 2001.
- [31] J. T. Davies and E.K. Rideal. *Interfacial Phenomena*. Academic Press New York and London, 1961.
- [32] *Optical Communication Systems*. Prentice/Hall International, 1983.
- [33] G. M. Hale and M. R. Querry. Optical constants of water in the 200-nm to 200-micrometer wavelength region. *Applied Optics*, 12(3):555–563, March 1973.
- [34] Photon Design. *FIMMWAVE Documentation (version 4.5)*, 2006.
- [35] COMSOL AB. *FEMLAB Electromagnetics Module User's Guide (Version 3.0)*, 2004.
- [36] Optiwave Systems Inc. *OptiFDTD Technical Background and Tutorials – Finite Difference Time Domain Photonics Simulation Software (version 6.0)*, 2005.
- [37] O. Parriaux and G. J. Veldhuis. Normalized analysis for the sensitivity optimization of integrated optical evanescent-wave sensors. *Journal of Lightwave Technology*, 16(4):573–582, April 1998.
- [38] Optiwave Systems Inc. *OptiBPM Technical Background and Tutorials – Waveguide Optics Modeling Software System (version 7.0)*, 2005.
- [39] Apollo Inc. *Apollo Photonic Solutions Suite User Manual*, 2002.
- [40] Optiwave Systems Inc. *OptiBPM User's Reference – Waveguide Optics Modeling Software System (version 7.0)*, 2005.

- [41] A. Wittkower, A. Auberton-Herve and C. Maleville. SMART-CUT(R) Technology for SOI: A new high volume application for ion implantation. In *Proceedings of the 2000 Conference on Ion Implantation Technology*, pages 269–272, Sept. 2000.
- [42] JEOL Ltd. <http://www.jeol.com>, August 2006.
- [43] Zeon Corporation. <http://www.zeon.co.jp>, August 2006.
- [44] S. Aachboun, P. Ranson, C. Hilbert and M. Boufnichel. Cryogenic etching of deep narrow trenches in silicon. *Journal of Vacuum Science and Technology A*, 18(4):1848–1852, 2000.
- [45] H. Jansen, M. de Boer, R. Legtenberg and M. Elwenspoek. The black silicon method: a universal method for determining the parameter setting of a fluorine-based reactive ion etcher in deep silicon trench etching with profile control. *Journal of Micromechanics and Microengineering*, 5(2):115–120, June 1995.
- [46] MicroChem Corp. <http://www.microchem.com>, August 2006.
- [47] SUSS MicroTec. <http://www.suss.com>, August 2006.
- [48] J. J. Fijol, E. E. Fike, P. B. Keating, D. Gilbody, J. J. LeBlanc, S. A. Jacobson, W. J. Kessler and M. B. Frish. Fabrication of silicon-on-insulator adiabatic tapers for low-loss optical interconnection of photonic devices. In *Proceedings of SPIE, Photonics Packaging and Integration III*, pages 157–170, 2003.
- [49] V. R. Almeida, R. R. Panepucci and M. Lipson. Nanotaper for compact mode conversion. *Optics Letters*, 28(15):1302–1304, August 2003.
- [50] Z. Lu and D. W. Prather. Total internal reflection-evanescent coupler for fiber-to-waveguide integration of planar optoelectric devices. *Optics Letters*, 29(15):1784–1750, August 2004.

- [51] G. Z. Masanovic, G. T. Reed, W. Headley, B. Timotijevic, V. M. N. Passaro, R. Atta, G. Ensell and A. G. R. Evans. A high efficiency input/output coupler for small silicon photonic devices. *Optics Express*, 13(19):7374–7379, 2005.
- [52] Aremco Products Inc. <http://www.aremco.com>, August 2006.
- [53] Buehler Ltd. <http://www.buehler.com>, August 2006.
- [54] Nanometrics Inc. <http://www.nanometrics.com>, August 2006.
- [55] D. B. Asay and S. H. Kim. Effects of adsorbed water layer structure on adhesion force of silicon oxide nanoasperity contact in humid ambient. *The Journal of Chemical Physics*, 124:174712-1–174712-5, 2006.
- [56] K. Hermansson, U. Lindberg, B. Hok and G. Palmskog. Wetting properties of silicon surfaces. In *Digest of Technical Papers, International Conference on Solid-State Sensors and Actuators*, pages 193–196, June 1991.
- [57] McGraw-Hill Encyclopedia of Science & Technology. *Boiling Point*. 2005.
- [58] J. A. McCaulley, V. M. Donnelly, M. Vernon and I. Taha. Temperature dependence of the near-infrared refractive index of silicon, gallium arsenide, and indium phosphide. *Physical Review B*, 49(11):7408–7417, 1994.
- [59] M. J. Adams. *An Introduction to Optical Waveguides*. John Wiley & Sons, 1981.
- [60] M. J. Robertson, P. C. Kendall, S. Ritchie, P. W. A. McIlroy and M. J. Adams. The weighted index method: a new technique for analyzing planar optical waveguides. *Journal of Lightwave Technology*, 7(12):2105–2111, December 1989.
- [61] F. Prieto, A. Llobera, D. Jimenez, C. Domenguez, A. Calle and L. M. Lechuga. Design and analysis of silicon antiresonant reflecting optical waveguides for evanescent field sensor. *Journal of Lightwave Technology*, 18(7):966–972, July 2000.

- [62] L. A. DeLouise and B. L. Miller. Trends in porous silicon biomedical devices – tuning microstructure and performance trade-offs in optical biosensors. In *Proceedings of SPIE, Optoelectronic Integration on Silicon*, pages 111–125, 2004.
- [63] D. Stroud. The effective medium approximation: some recent developments. *Superlattices and Microstructures*, 23(3–4):567–573, 1998.
- [64] H. F. Arrand. *Optical waveguides and components based on porous silicon*. PhD thesis, University of Nottingham, 1997.
- [65] A. M. Tinsley-Bown, L. T. Canham, M. Hollings, M. H. Anderson, C. L. Reeves, T. I. Cox, S. Nicklin, D. J. Squirrell, E. Perkins, A. Hutchinson, M. J. Sailor and A. Wun. Tuning the pore size and surface chemistry of porous silicon for immunoassays. *Physica Status Solidi (A)*, 182(1):547–553, 2000.